# Deep regolith weathering controls $\delta$30Si composition of groundwater under contrasting landuse in tropical watersheds

Sarath Pullyottum Kavil, Jean Riotte, Ramananda Chakrabarti, Arnaud Dapoigny, Véronique Vaury, Laurent Ruiz, Damien Cardinal

Chemical Geology 670 (2024) 122370

Contents lists available at ScienceDirect

Chemical Geology

journal homepage: www.elsevier.com/locate/chemgeo

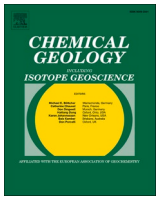

# Deep regolith weathering controls $\delta^{30}Si$ composition of groundwater under contrasting landuse in tropical watersheds

Sarath Pullyottum Kavil [a,i,*], Jean Riotte [b,f], Ramananda Chakrabarti [c,d], Arnaud Dapoigny [e], Véronique Vaury [h], Laurent Ruiz [f,g], Damien Cardinal [a]

[a] LOCEAN-IPSL, Sorbonne Universite-IRD-CNRS-MNHN, Paris, France
[b] GET-OMP, IRD, Toulouse, France
[c] Centre for Earth Sciences, Indian Institute of Science, Bangalore, India
[d] Interdisciplinary Centre for Water Research, Indian Institute of Science, Bangalore, India
[e] Laboratoire des Sciences du Climat et de l'Environnement, LSCE-IPSL, CEA-CNRS-UVSQ-Université Paris-Saclay, F-91191 Gif-sur-Yvette, France
[f] Indo-French Cell for Water Sciences, ICWAR, IRD, Indian Institute of Science, Bangalore, India
[g] G-EAU, INRAE - AgroParisTech - Cirad - IRD - Montpellier SupAgro - Univ Montpellier, Montpellier, France
[h] IEES, Sorbonne Université, Paris, France
[i] Now at department of Geological Sciences, Stockholm University, Sweden

ARTICLE INFO

Editor: Oleg Pokrovsky

*Keywords:*
Groundwater
Weathering
Silicon cycle
Forest
Agriculture
Critical zone

ABSTRACT

Land use changes are known to alter terrestrial silicon cycling and the export of dissolved silicon from soil to fluvial systems, but the impact of such changes on groundwater systems remain unclear. In order to identify the processes responsible for groundwater geochemistry and to assess the impact of agricultural processes, we examined multiple isotopic tracers ($\delta^{30}Si$, oxygen ($\delta^{18}O$) and hydrogen ($\delta^{2}H$) isotopes) in groundwater, soil porewater and surface water from two contrasted watersheds having the same gneissic lithology, one forested (Mule Hole) and one intensely cultivated (Berambadi) in the Kabini basin in South India. In the cultivated watershed, groundwater exhibits high $Cl^-$ and $NO_3^-$ concentrations indicative of fertilizer inputs and solute enrichment from evapotranspiration due to multiple groundwater pumping/recharge cycles. The DSi concentration in groundwater is significantly higher in the cultivated watershed (980 ± 313 μM) than in the forested one (711 ± 154 μM), indicating more intense evapotranspiration due to irrigation cycles. The groundwater $\delta^{30}Si$ values ranged from 0.6 ‰ to 3.4 ‰ and exhibit no significant differences between cultivated (1.2 ± 0.5 ‰) and forested (1.0 ± 0.2 ‰) watersheds, indicating limited impact of land use and land cover. Groundwater also shows no significant seasonal differences in DSi and $\delta^{30}Si$ within watersheds, indicating a buffer to seasonal recharge during wet season. The $\delta^{30}Si$ of a majority of groundwater samples fits a steady-state open flow through system, with an isotopic fractionation factor ($^{30}\varepsilon$) between precipitating phase and groundwater ranging from −1.0 ‰ and − 2.0 ‰, consistent with precipitation of kaolinite-type clays, dominant in the study area. The steady-state flow through system in groundwater can be interpreted as a continuous DSi input from mineral weathering reactions with a dynamic equilibrium between Si supply and precipitation of secondary phases. We also observe, in both watersheds, similar DSi and $\delta^{30}Si$ values in local surface water that includes small streams and a river (406 ± 194 μM, 1.6 ± 0.3 ‰) and in soil porewater (514 ± 119 μM, 1.6 ± 0.2 ‰). Compared to soil porewater, groundwater exhibits significantly lower $\delta^{30}Si$ signatures and higher DSi, reflecting the contribution of an isotopically light silicon source, resulting from water-rock interaction during percolation through the unsaturated zone. We assign this steady input of DSi to the weathering of primary silicate minerals in the regolith, such as Na-plagioclase, biotite and chlorite, with formation of kaolinite and smectites type clays. A simple isotopic mass balance suggests that deep regolith weathering can contribute to almost half of the DSi in groundwater. We conclude that silicon cycling in soil porewaters, and surface waters are directly impacted by land use, while the isotopic composition of groundwater remains unaffected. Our results indicate that Si isotopic signatures of weathering, adsorption, and plant uptake occurring in the shallow soil and saprolite horizons are

* Corresponding author at: LOCEAN-IPSL, Sorbonne Universite-IRD-CNRS-MNHN, Paris, France.
*E-mail address:* sarath.pullyottum.kavil@geo.su.se (S.P. Kavil).

https://doi.org/10.1016/j.chemgeo.2024.122370
Received 1 May 2024; Received in revised form 10 August 2024; Accepted 29 August 2024
Available online 30 August 2024

partly overprinted and homogenized by the regolith weathering in the deep critical zone, irrespective of land use and seasonality.

## 1. Introduction

Silicon (Si) second most abundant element in Earth's crust and terrestrial weathering mobilizes Si as dissolved silicon in the form of silicic acid ($H_4SiO_4$, thereinafter referred to as DSi), which is transported to the ocean through fluvial systems. It is one of the essential nutrients which plays a critical role in the growth and distribution of highly productive autotrophs such as diatoms in both freshwater and marine ecosystems (Street-Perrott and Barker, 2008; Tréguer et al., 2021). Land cover and land use changes are one of the major drivers of Si cycling at the global scale (Conley et al., 2008; Struyf et al., 2010; Carey and Fulweiler, 2016). Silicon is considered as a quasi-essential element for many plants and can be found in all photosynthetic plants, with concentration ranging from 0.1 to over 10 % by dry weight (Epstein and Epstein, 2009). Plants can take up DSi from soil solution and precipitate it as biogenic silica (amorphous $SiO_2.nH_2O$, hereafter referred to as BSi), in the form of siliceous bodies in cell walls known as phytoliths (Alexandre et al., 1997; Epstein and Epstein, 2009). Although Si export through crop harvesting is known to deplete Si pools in soil, the extent to which agriculture impacts the export of Si from soil to hydrosystems remains to be understood (Ding et al., 2008; Vandevenne et al., 2015). The stable isotopic composition of Si, expressed as per mil deviation from standard ($\delta^{30}$Si values), is a useful tool to evaluate sources and processes controlling Si biogeochemical cycling (Cornelis et al., 2011; Opfergelt and Delmelle, 2012; Frings et al., 2016 and references therein). The Si solubilized by chemical weathering of the source bedrock (bulk upper continental crust $\delta^{30}$Si value of $-0.25 \pm 0.16$ ‰, Savage et al., 2014) undergoes fractionation during incorporation into secondary phases, which favors the lighter $^{28}$Si isotope, thereby making the residual solutions (soil waters, groundwaters and rivers) enriched in the $^{30}$Si isotopes (Frings et al., 2016). The isotopic fractionation ($^{30}\varepsilon$) during precipitation of secondary clays depends on the clay mineral groups, ranging from −1 ‰ in smectite type clays and up to −3.0 ‰ in kaolinites (Frings et al., 2021). The silicon uptake by plants is also associated with preferential incorporation of the lighter $^{28}$Si isotope, followed by further fractionation during translocation, depleting the $^{28}$Si from root to leaves with an overall associated $^{30}\varepsilon$ between 0 ‰ to −2.0 ‰ for different plant species (Opfergelt et al., 2006; Frick et al., 2020; Frings et al., 2021). Thus, careful evaluation of Si interaction with the lithosphere, biosphere and hydrosphere components is essential to understand output fluxes of Si at the watershed scale, and its subsequent transfer to the oceans. One such evaluation across a land use gradient in a temperate climate of Western Europe showed a significant enrichment in $^{30}$Si of soil water from cropland intensively cultivated for almost 240 years, compared to that from a forested landscape (Vandevenne et al., 2015). This isotopic difference was also reflected in the $\delta^{30}$Si of DSi exported to the estuary by the streams of the studied sub-watersheds (Delvaux et al., 2013). However, the chemical composition of streams and rivers do not reflect the composition of groundwater, in particular where deep unsaturated regolith acts as a subsurface reservoir (Riotte et al., 2018a). The fate of Si in pore water as it travels through the unsaturated zone, often with long residence time, before reaching groundwater systems is critical in understanding output fluxes from the watershed. Existing groundwater $\delta^{30}$Si values span over a wide range, from −1.5 to +2.6 ‰ ($n = 66$, Georg et al., 2009a, 2009b; Pogge von Strandmann et al., 2014; Frings et al., 2016; Ehlert et al., 2016; Martin et al., 2021), which is attributed to silicate weathering and dissolution of lighter sources of Si such as secondary minerals. However, the impact of landuse changes and soil processes on groundwater Si cycling and the response to seasonal precipitation changes remains unclear.

India accounts for one third of the world's total irrigated area and about 60 % of irrigation results from groundwater pumping, leading to rapid decline of the groundwater levels (Thenkabail et al., 2009; Fishman et al., 2011; Bhaduri et al., 2012). Aquifers in peninsular India are unconfined and composed of fractured granitic bedrock having a decreasing transmissivity with depth (Dewandel et al., 2006), which limits the area under irrigation from a well to <1 ha (Fishman et al., 2011). Such tube wells are ideal for small farmers dominating Indian agriculture, leading to a high density of farm tube wells in the past few decades. Intense pumping for agricultural as well as domestic purposes has led to deterioration of the groundwater quality and deepening of water table (Rodell et al., 2009; Buvaneshwari et al., 2017). Intense pumping and irrigation from borewells and handpumps can lead to groundwater recycling through return flow in cultivated landscapes, which can potentially increase the DSi in soil solutions and groundwater through evapotranspiration. This, along with excessive use of fertilizers and organic manures can significantly alter the chemical and isotopic composition of groundwater (Buvaneshwari et al., 2017, 2020; Robert et al., 2017). However, the isotopic impact of such irrigation practices is not well understood. Despite growing evidence of human impacts on groundwater hydrogeochemistry, we lack a clear understanding of how the signatures of surface and subsurface processes get transferred to deep groundwater. The existing $\delta^{30}$Si values of rivers, soil solution and groundwater open up two possible hypotheses; *i)* crop cultivation and groundwater irrigation practices can increase the $\delta^{30}$Si values of soil solution through plant uptake, which is reflected on groundwater as high $\delta^{30}$Si value of agriculture watershed, *ii)* despite significant alteration of soil processes and ecosystem functioning, signatures of land use are overwritten through soil and saprolite processes, and not reflected in groundwater. In the current study, we present a novel dataset of silicon concentration and $\delta^{30}$Si of groundwater, soil solution and surface streams and a river from two watersheds under contrasting land use, forest and irrigated agriculture, in South India. We complement the dataset with hydrochemistry and water isotopes to understand the drivers of groundwater chemistry and address three major questions*; i)* how does the $\delta^{30}$Si signatures evolve as soil water get transferred to groundwater systems? *ii)* can irrigated agriculture and seasonal monsoonal precipitation alter the silicon isotopic signatures in groundwater? *iii)* What controls the silicon isotopic composition in groundwater? Through extensive sampling of groundwater and surface water, we aim to bridge the gap between shallow and deep soil processes affecting Si signatures in groundwater.

## 2. Materials and methods

### 2.1. Study area, lithology, and climate

We studied two contrasting watersheds in Southern India: the agricultural watershed of Berambadi (84 km$^2$) and the pristine forested watershed of Mule Hole (4.1 km$^2$), both belonging to the Kabini Critical Zone Observatory, the Indian site of the M-TROPICS observatory (Sekhar et al., 2016; Riotte et al., 2021a, 2021b), part of the OZCAR research infrastructure (Gaillardet et al., 2018) (Fig. 1). Local climate is driven by a double monsoon system, South-West monsoon (June–September) and North-East monsoon (October–December). The bedrock of both watersheds is dominated by Precambrian peninsular gneiss (85 %) and intermingled with minor mafic to ultramafic rocks (15 %, includes hornblende, amphibolite, and serpentinite) (Naqvi and Rogers, 1987). Major minerals in the gneiss include quartz, albite, sericite, biotite-chlorite with accessory minerals such as apatite, epidote, allanite titanite, magnetite, ilmenite, pyrite and zircon (Braun et al., 2009). The upper porous clayey to loamy regolith layers, with high porosity and low

permeability, is underlaid by fissured bedrock, mainly assuming a transmissive function of the aquifer, forming the hard rock aquifer typical of the region (Dewandel et al., 2006; Soumya et al., 2011). The thickness of weathered bedrock, also called as regolith, in both watersheds ranges from 0 to 30 m with an average of 17 m (Braun et al., 2009). The regolith is composed of 15 m of immature saprolite and a 2 m thick ferralsols (88 %) or vertisols (12 %) layer on top (FAO-ISRIC-ISSS, 1998, Barbiéro et al., 2007; Braun et al., 2009). Primary minerals such as quartz, albite, sericite, chlorite and hornblende predominate the saprolite minerology with kaolinite, smectite and Fe-oxyhydroxides occurring as secondary phases (Braun et al., 2009; Violette et al., 2010). The dominant weathering reaction in the watershed is Na-plagioclase weathering (38 % abundance in bedrock) and formation of kaolinite-type clay minerals (Braun et al., 2009; Riotte et al., 2018a).

The Mule Hole watershed is located under sub-humid tropical climate, receiving a mean annual rainfall of 1100 mm distributed from March to November (Gunnell and Bourgeon, 1997). The temperature ranges between 37 °C during summer and 17 °C during the peak winter, typically in January. The watershed has been preserved from any human activities since 1974, as it belongs to the Bandipur national park (Maréchal et al., 2009). Hydrological mass balance in the watershed suggests that groundwater recharge is dominated by two components; i) direct recharge from rainfall distributed over the watershed (45 mm/yr), ii) indirect recharge during stream storms by infiltration from the streambed (30 mm/yr) (Maréchal et al., 2009). In the semi-arid Berambadi watershed, 60 % of the total area is used for agriculture. The remaining 40 %, located in the West (upstream) are part of the Bandipur park (Buvaneshwari et al., 2017). Pedoclimatic conditions are similar to Mule Hole with, however, slightly lower rainfall (800–900 mm/yr). In the watershed valley, the number of bore wells is particularly high, more than 1000. Groundwater undergoes intense pumping which causes lowering of the groundwater table depth and large seasonal and interannual fluctuations depending on rainfall and pumping intensity. Most of the groundwater samples of the present study were collected from actively pumped tube wells in cultivated fields. Increase in the number of tube wells from 1990s led to a shift from low water demand rainfed crops like finger millet, sorghum and pulses to groundwater irrigated agriculture with high water demand cash crops such as sugarcane (*saccharum officinarum*), banana (*musa acuminata*), turmeric (*curcuma longa*) and vegetables (Sekhar et al., 2016; Fischer et al., 2022). At the time of sampling (2019), groundwater exhibited an enhanced groundwater hydraulic gradient, with the upstream (western) part having shallow groundwater levels and deeper groundwater downstream (eastern) (Fig. 1, Buvaneshwari et al., 2017).

### 2.2. Sampling and analyses

We sampled groundwater and surface water including small streams and river, in 2019, in March for the dry season and August for the monsoon season. In Mule Hole, groundwater samples were collected from 9 observation wells drilled in 2003 and 2004 (Fig. 1). Three wells P3, P5 and P6 are located along the watershed boundary (300–400 m to the nearest stream), far from the stream to monitor the background characteristics of the aquifer and fluctuations in hydraulic gradient within the watershed. The remaining six wells lie in a straight line perpendicular to the stream axis at its outlet with P1 and P7 very near to the stream. In Berambadi, groundwater samples were collected from borewells and handpumps at 17 locations within the watershed. Groundwater levels (groundwater table depth) were measured before sampling using a manual piezometric level sensor (Skinny Dipper device, Haron Instruments), except for handpumps, where such measurement is impossible, and for which the groundwater table depth was assumed to lie within 5 m. Groundwater table depths ranged from 1.6 m in shallow groundwater in Mule Hole to almost 46 m below ground level

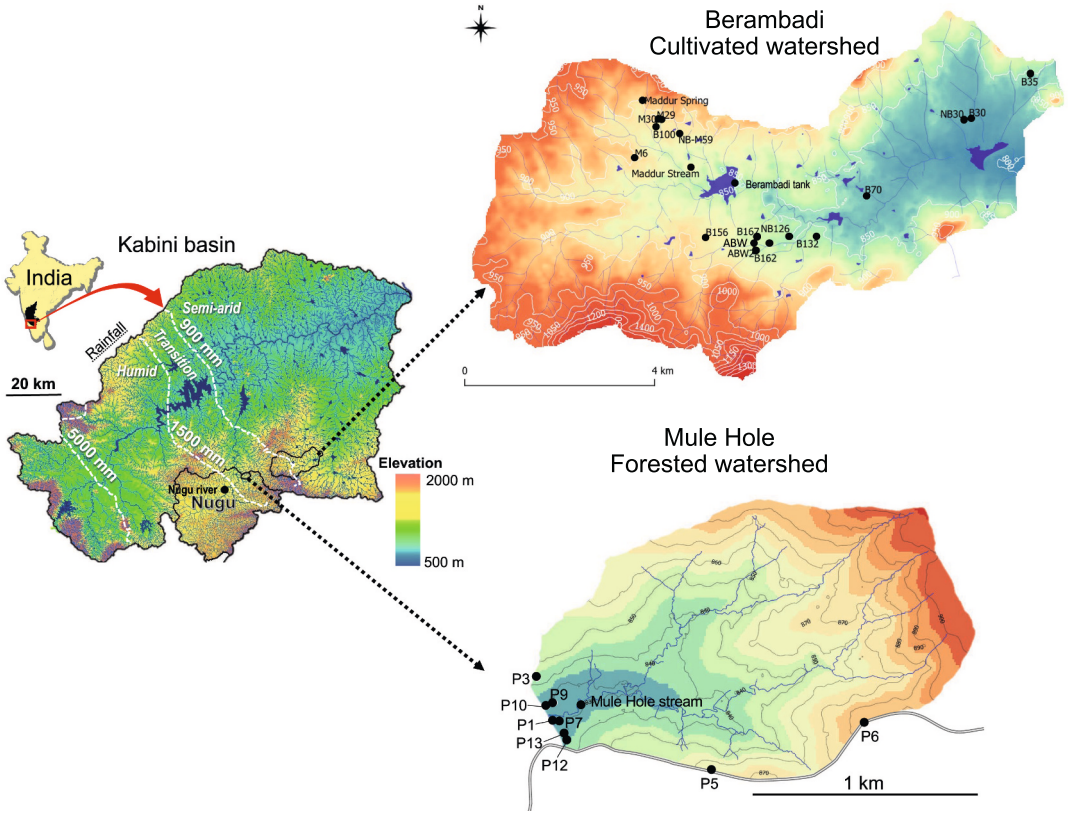


**Fig. 1.** Kabini watershed map with elevation, precipitation levels (mm/yr) and climatic zones are demarcated using dashed white lines. The two watersheds sampled for the current study; the cultivated Berambadi watershed and forested Mule Hole watershed. The sampling locations of groundwater and surface water samples are marked in Mule Hole and Berambadi.

(bgl) in Berambadi. Prior to sample collection, all sampled wells were purged until the pH and conductivity were stabilized. The sampling also included borewells which were not actively pumped due to low groundwater yield (for e.g. abandoned bore well (ABW)). Surface water samples consisted in the Nugu river (tributary of Kabini river draining mostly the humid zones) and in Berambadi few ephemeral streams and a tank, filled during seasonal rainfall, very close to the groundwater sampling locations. Soil porewaters of the Berambadi watershed were collected in March 2015 by members of the Indo-French cell, Indian Institute of Science (IISc), using soil porewater samplers (*Rhizon*®) from depths ranging from 5 to 60 cm. The rainwater samples were collected between April 2005 and May 2006 during an earlier field campaign near Mule Hole, about 1 km from stream outlet. All water samples were filtered just after collection using 0.4 μm SUPOR® PES filters, and aliquots for various analyses were stored in acid rinsed containers. The aliquot for major cation analysis was acidified with few drops of double distilled $HNO_3$ and the unacidified aliquot was used for DSi and Si isotope analysis. Additionally, an aliquot for water isotopes ($\delta^2H$ and $\delta^{18}O$) was collected and stored in 10 ml glass tubes.

### 2.3. Elemental concentrations

Major cation and anion concentrations were measured with an Ion Chromatograph (Metrohm COMPACT 861) at the Indo-French Cell for Water Sciences (IFCWS, Indian Institute of Science, India (IISc)). The accuracy of measurements was monitored using multiple certified reference materials (AnionWS, ION-96.4, ION 915, SUPER-05 and BIG MOOSE 02) and the external reproducibility was better than 5 %.

Trace element concentration (Al, Sr, Fe, Mn) were determined by quadrupole inductively coupled plasma mass spectrometry (ICPMS, 7500cx Agilent) at the Alysés analytical platform (IRD-Sorbonne Université, Bondy, France). Samples and standards were diluted and measured in 2 % $HNO_3$. The accuracy of the analyses was assessed by measuring certified natural water reference standard SLRS-6 (National Research Council of Canada) and average precision for trace element analysis was within 10 %.

### 2.4. Water isotope analysis

The hydrogen and oxygen stable isotopic composition (measured as $\delta^2H$ and $\delta^{18}O$) of water samples were determined by a stable isotope ratio mass spectrometer (Picarro L2130-i Isotopic Water Analyzer, IEES, Paris, LSCE-IPSL, Gif-sur-Yvette, Paris and LEFE in Toulouse). The results are reported in per mil (‰) deviation with respect to the Vienna Standard Mean Ocean Water (VSMOW2). The analytical uncertainty was estimated from the repeated measurements of the Picarro MID standard reference, at ±0.1 ‰ for $\delta^{18}O$ and ± 0.5 ‰ for $\delta^2H$, respectively.

### 2.5. Dissolved silicon and silicon isotope analysis

The dissolved silicon concentration (DSi) was measured by spectrophotometry following the protocol of Grasshoff et al. (1999). The accuracy of the analyses was assessed using the certified reference material PERADE 09 (supplied by Environment Canada, lot no:0314, with DSi = 110.0 ± 6.8 μM), during each analytical session giving a mean reproducibility of 110 ± 3 μM ($n = 25$). For Si isotope analysis, we followed a slightly modified two-step pre-concentration method adapted from MAGIC (Magnesium coprecipitation technique, Karl and Tien, 1992; Reynolds et al., 2007; Hughes et al., 2011). To an initial volume of 10 ml of water samples, we added 0.5 ml of $MgCl_2$ solution to match the seawater Mg concentration and 2 % (*v*/v) of 1 M NaOH, shaken and kept undisturbed overnight. The brucite ($Mg(OH)_2$) precipitated at high pH scavenges Si. The supernatant from the first step was again subjected to a second addition of 1 % NaOH, and the new precipitate was recovered by centrifugation (at 2500 rpm for 10 min) after 1–2 h. Brucite precipitates from both steps were dissolved with 1 M HCl and merged. The DSi concentration of the supernatant was analyzed by spectrophotometer (Grasshoff et al., 1999) and found to be negligible (on average < 2 %), confirming that Si was almost completely adsorbed onto the brucite precipitate.

Prior to Si isotope analysis, cations were removed from the solution using cation exchange resin (BioRad DOWEX 50 W-X12, 200 to 400 mesh, in $H^+$ form) following the procedure of Georg et al. (2006a, 2006b). After the purification process, an aliquot was analyzed for major element concentrations (Na, Mg, Ca, K) by ICP-MS (Agilent 7500a) to ensure that the Si/X (Where X = Na, K, Ca or Mg) weight ratio is always >50 to minimize matrix effects in the plasma. The organic matrix was removed by oxidizing the residue with 50 μl of 30 % $H_2O_2$, thereby to avoid potential matrix bias during isotopic analysis (Hughes et al., 2011). Analyses performed on a series of 35 groundwater and surface water samples showed that the preconcentration and $H_2O_2$ treatment increased the DSi/DOC ratio from 18 to 7000 times, with DSi/DOC ratio > 10 in all final aliquots. The procedure ensured <0.2 ‰ isotopic mass bias due to DOC matrix (Hughes et al., 2011). The possible remaining matrix effect resulting from the $Cl^-$, $NO_3^-$ and $SO_4^{2-}$ was corrected by the artificial doping of all the samples and standards with Suprapur grade 0.5 M $HNO_3$, 0.5 M HCl, 1 mM $H_2SO_4$ (Merck, Hughes et al., 2011). The measurements were performed on a MC-ICP-MS (Thermo Neptune+, LSCE-IPSL, Gif-sur-Yvette) in dry plasma mode with Mg internal standard to correct for the instrumental mass bias as described by Closset et al. (2016). Samples were injected into the plasma with an ApexΩ HF desolvating nebulization system connected with a PFA nebulizer (100 μl/min uptake rate). Results were expressed in the delta notation ($\delta^{30}Si$) as the per mil (‰) deviation from the standard material NBS 28 (Eq. (1)):

$$\delta^{30}Si_{sample} = \left[ \frac{\left(^{30}Si/^{28}Si\right)_{sample}}{\left(^{30}Si/^{28}Si\right)_{NBS28}} - 1 \right] \times 1000 \quad (1)$$

Blank levels were below 1 % of the main signal and were subtracted from each sample and standard analysis. All measurements were carried out in medium-resolution mode ($m/\Delta m > 6000$) to optimize the separation of $^{30}Si$ peak and $^{14}N^{16}O$ interference and were performed on the interference-free left side of the peak (Abraham et al., 2008). The $\delta^{29}Si$ and $\delta^{30}Si$ values were compared to the mass-dependent fractionation line and samples falling outside the line were excluded from the final dataset. Typical analytical conditions are provided in Table S1. The analytical precision and accuracy were monitored by the long-term measurements of a second reference material, diatomite, which yielded an average $\delta^{30}Si$ value of 1.19 ± 0.18 ‰ (2SD, $n = 100$), not significantly different from the reference value of 1.26 ‰ (Reynolds et al., 2007). Diatomite solutions processed with MAGIC preconcentration, and cation chromatography provided an average $\delta^{30}Si$ value of 1.1 ± 0.1 ‰ (2SD, $n = 12$) which within our analytical reproducibility. All samples measured in the present study were chemically replicated at least once, including the MAGIC preconcentration and cation chromatography (average variability of 0.05 ± 0.15 ‰), and 23 samples were triplicated (average 2SD of ±0.2 ‰).

### 2.6. Data handling

#### 2.6.1. Atmospheric input and fertilizer $Cl^-$ correction

In pristine watersheds, the contribution of atmospheric input is estimated using $Cl^-$, assuming all the $Cl^-$ originate from rainwater and normalizing the rainwater composition to $Cl^-$ (Gaillardet et al., 1999). The rainwater corrected concentration for a given element is calculated as:

$$[X^*] = [X]_{measured} - \left(X/Cl^-\right)_{rain}{}^{*}[Cl^-]_{measured} \quad (2)$$

Here, [X*] represents the atmosphere-corrected concentration of the element of interest, $[X]_{measured}$ is the measured concentration of element

in groundwater, $(X/Cl^-)_{rain}$ represents the ratio of element X and $Cl^-$ in rainwater and $[Cl^-]_{measured}$ is the groundwater chloride concentration (Riotte et al., 2014). In cultivated watersheds, such as Berambadi, solutes in groundwater originate from atmospheric inputs, mineral weathering, and fertilizer. In Berambadi, potash (KCl) fertilization is widespread and the above correction is not applicable. To estimate the $Cl^-$ contribution from KCl, we followed the deconvolution method proposed by Buvaneshwari et al. (2020), based on relative proportions of $Na^+$ and $Cl^-$ and using pristine Mule Hole watershed as a reference. The correction assumes that release of Na during mineral weathering is similar for both watersheds and $Na^+$ and $Cl^-$ are conservative in the system (see Buvaneshwari et al., 2020 for more details). Following which, the atmospheric input correction for major cations except that Na in groundwater was performed based on Eq. 2 using fertilizer-corrected $Cl^-$ ($Cl^{\#}$) (see Table 1). Given the low DSi content in rainwater, the atmospheric correction of groundwater DSi is considered negligible (Riotte et al., 2014).

#### 2.6.2. Bedrock normalization and modeling of $\delta^{30}Si$ evolution in water

To estimate the fraction of Si released as DSi during weathering, we adopted the normalization proposed by Georg et al. (2007), where DSi of groundwater was first normalized to a reference element, Na in our case because it originates only from primary silicate minerals (mostly Na-plagioclase) and it is not incorporated into secondary phases. Following which, the Si/Na ratio in water samples was normalized to that of the gneissic bedrock (Si content in the gneiss itself corrected for inert quartz and sericite contents, Braun et al., 2009) to obtain a proxy for weathering congruency.

$$f_{Si} = Si/Na_{groundwater}/Si/Na_{bedrock} \quad (3)$$

A $f_{Si}$ of 1 corresponds to the congruent dissolution of the bedrock, i.e., 100 % of the Si mobilized by silicate weathering stays in the dissolved phase with a $\delta^{30}Si$ identical to that of the bedrock. The $f_{Si}$ decrease corresponds to the progressive incorporation of Si into secondary phases, such as clay precursors and plant phytoliths (Ziegler et al., 2005; Fernandez et al., 2022). The DSi removal from groundwater systems may follow two modelled scenarios, that will influence the silicon isotopic signatures; i) a Rayleigh model, where solution is assumed to be isolated from the precipitating solids without any further exchange (Eq. 4), ii) a steady-state open flow through batch reactor model (here onwards steady state model) where supply of fresh Si into the system is balanced by precipitation and export of secondary solids (Eq. 5) (Bouchez et al., 2013; Frings et al., 2015).

$$\text{Rayleigh}: \delta^{30}Si_{mea} = \delta^{30}Si_o + {}^{30}\varepsilon \times ln(f_{Si}) \quad (4)$$

$$\text{Steady state}: \delta^{30}Si_{mea} = \delta^{30}Si_o - {}^{30}\varepsilon \times (1 - f_{Si}) \quad (5)$$

Here $f_{Si}$ indicates the fraction of DSi remaining in the groundwater, obtained by Eq. 3. The $\delta^{30}Si_{mea}$ value denotes the $\delta^{30}Si$ measured in groundwater and surface water samples and $\delta^{30}Si_o$ denotes the initial $\delta^{30}Si$, which is the granitic gneiss bedrock value of $-0.34 \pm 0.08$ ‰ (Riotte et al., 2018a). The ${}^{30}\varepsilon$ is isotopic fractionation, defined as ${}^{30}\varepsilon = \alpha$-1, expressed in per mil (‰), where α is the isotopic fractionation factor associated with secondary mineral precipitation or plant uptake.

## 3. Results

### 3.1. Chemical composition of water samples

Characteristics and chemical composition of groundwater and surface water samples are provided in Table 1. The groundwater table depth in the sampled wells ranged between 1.5 and 46 m. The groundwater table depth fluctuated in both watersheds across season, with some wells showing deeper water levels during wet season and others during dry season. The pH of the groundwater varied between 5.8 and 7.8, with only few Berambadi groundwater showing a slightly alkaline nature. Average electrical conductivity in Berambadi groundwater was $1500 \pm 578$ μS/cm ($n = 33$, 1SD), almost twice as that of Mule Hole ($553 \pm 201$ μS/cm, 1SD). There was no significant seasonal difference observed in conductivity between dry and wet season within a watershed (*t*-test, Table 1, Fig. S1). Berambadi groundwater exhibited an average $Cl^-$ concentration of $4700 \pm 3800$ μM, one order of magnitude higher than in Mule Hole. For Berambadi groundwater samples, fertilizer contribution accounted on average for $75 \pm 25$ % of the total $Cl^-$ content. The molar concentration of anions in groundwater of both watersheds decreased in the order, $[HCO_3^-] > [Cl^-] > [SO_4^{2-}]$. Concentrations of anions such as $Cl^-$, $NO_3^-$, $PO_4^{3-}$ and $SO_4^{2-}$ increased with conductivity, with Berambadi groundwater exhibiting significantly higher nitrate concentration compared to Mule Hole (Fig. S1). The cationic load in both watersheds was dominated by $Na^+$, followed by $Ca^{2+}$ and $Mg^{2+}$, covarying with measured conductivity. Potassium accounted for only a small part of the cationic load despite higher content in fertilizers, suggesting that most of it was incorporated in crops or immobilized in soils. Atmospheric input accounted for less than 20 % of the cation load in both watersheds (Table 1, atmospheric input corrected values are given in asterisk). We observe higher conductivity and sum of cations in deep groundwater (≥10 m) compared to shallow groundwater (<10) from both watersheds, but was significant only in Berambadi watershed (*p-value* < 0.05, Table 1).The surface water from small streams exhibited solute concentration similar to the groundwater next to it, while the Nugu river, which partly drains the humid zone of the Kabini basin, exhibited a much more dilute elemental load. Most of the groundwater samples exhibited Al, Fe, and Mn concentrations <1 μM with a few outliers corresponding to samples collected from shallow handpumps and piezometers (Table 1).

### 3.2. Water isotopes

The isotopic composition of groundwater and surface water in Berambadi and Mule Hole are given in Table 2. Stable water isotopic composition of Berambadi groundwater ranged from −1.7 ‰ to −3.8 ‰ for $\delta^{18}O$ and from −8.9 ‰ to −21.6 ‰ for $\delta^2H$, respectively. In Mule Hole groundwater $\delta^{18}O$ ranged from −1.7 to −3.7 ‰ and $\delta^2H$ from −2.1 to −18.1 ‰, respectively. The local meteoric water line (LMWL), derived from rainwater water isotope data from Mule Hole (Fig. 2, details of rainwater in Table S2) exhibited a slope similar to that of the global meteoric water line (GMWL, Craig, 1961). The deuterium excess (d-excess = $\delta^2H$-8*$\delta^{18}O$) showed consistently lower values in Berambadi compared to Mule Hole and exhibited a general negative trend with conductivity (Fig. S1). We observe no seasonal variability in the water isotopic signature of groundwater, suggesting significant buffering of seasonal variations in monsoonal rainfall isotopic signature as previously documented by Warrier et al. (2010).

### 3.3. Dissolved silicon (DSi) and $\delta^{30}Si$

The average DSi of groundwater water was significantly higher in Berambadi ($980 \pm 313$ μM, 1SD, $n = 33$) than in Mule Hole watershed ($711 \pm 154$ μM, 1SD, $n = 18$) (*p* value<0.05, Tables 1, 2, Fig. 3) during both dry and wet season. The surface waters, including the Nugu river, showed a lower DSi compared to groundwater with an average of $427 \pm 194$ μM (1SD, $n = 8$). The groundwater DSi of the region was generally higher than the average estimate for extrusive igneous ($604 \pm 192$ μM) and granitic ($334 \pm 255$ μM) bedrocks (Rahman et al., 2019). Dissolved $\delta^{30}Si$ of the groundwater ranged from 0.6 ‰ to 3.4 ‰ and was enriched in heavy isotope compared to bulk upper continental crust value ($-0.25 \pm 0.16$ ‰, Savage et al., 2014) and to the local gneiss value reported for Mule Hole ($-0.34 \pm 0.08$ ‰, Riotte et al., 2018a). The $\delta^{30}Si$ of groundwater from an abandoned borewell (ABW) in Berambadi watershed is the heaviest ever measured in groundwater so far, exhibiting a value of 2.9 ‰ and 3.5 ‰ for dry and wet season, respectively. Overall,

**Table 1**
The sample details, groundwater table depth (m), conductivity and elemental composition of groundwater and surface water from Berambadi and Mule Hole. The # denote the Cl concentration corrected for fertilizer input in Berambadi, the correction is not applicable to pristine Mule Hole watershed (see section 2.5.1 for details).

| | | Depth | pH | Conductivity | DSi | Na | K | Ca | Mg | Sr | Al | Mn | Fe | Cl | Cl# | $NO_3$ | $PO_4$ | $SO_4$ |
|---|---|---|---|---|---|---|---|---|---|---|---|---|---|---|---|---|---|---|
| | | m | | µS/cm | µM | µM | µM | µM | µM | µM | µM | µM | µM | µM | µM | µM | µM | µM |
| **Berambadi** | | | | | | | | | | | | | | | | | | |
| *Dry season* | | | | | | | | | | | | | | | | | | |
| ABW | Piezometer | 6.5 | 7.9 | 786 | 111 | 3031 | 112 | 552 | 2105 | 2.3 | 0.2 | 5.0 | <dl | 773 | 529 | 13 | 25 | 294 |
| ABW2 | Piezometer | 6.0 | 7.3 | 1423 | 1150 | 4001 | 13 | 1517 | 3830 | 12.5 | 0.2 | <dl | 0.1 | 2196 | 698 | 1995 | 51 | 511 |
| B100 | Borewell | 4.5 | 7.1 | 1890 | 1000 | 11595 | 69 | 1678 | 1502 | 11.8 | 0.2 | <dl | 0.1 | 7580 | 2024 | 1779 | n.a | 378 |
| B132 | Borewell | 10.0 | 6.9 | 2030 | 1054 | 2991 | 148 | 3986 | 5399 | 25.3 | 0.2 | <dl | <dl | 7999 | 522 | 2664 | 80 | 712 |
| B156 | Borewell | 5.1 | 7.3 | 1501 | 995 | 3368 | 107 | 1669 | 3351 | 11.7 | 0.4 | 0.1 | 0.2 | 4312 | 588 | 1847 | 47 | 503 |
| B167 | Borewell | 9.4 | 7.2 | 1011 | 966 | 1768 | 48 | 2336 | 2154 | 6.7 | 0.2 | 0.0 | 0.1 | 1428 | 309 | 1503 | 45 | 258 |
| B30 | Borewell | 46.0 | 6.8 | 2310 | 1301 | 4224 | 1069 | 5761 | 3561 | 17.2 | 0.4 | 0.0 | 0.1 | 8267 | 737 | 6085 | 82 | 1603 |
| B35 | Piezometer | 36.3 | 6.8 | 892 | 1435 | 2660 | 165 | 1841 | 1600 | 6.0 | 0.4 | 0.2 | <dl | 464 | 464 | 759 | 34 | 190 |
| B70 | Borewell | 34.5 | 6.8 | 2460 | 1060 | 7810 | 188 | 6313 | 2302 | 18.7 | 0.3 | 0.0 | <dl | 12219 | 1363 | 2688 | 72 | 1845 |
| M29 | Handpump | 5.0 | 7.0 | 1336 | 583 | 4857 | 296 | 2997 | 1825 | 10.6 | 0.2 | 6.0 | 25.4 | 5707 | 848 | 102 | 44 | 291 |
| M30 | Handpump | 5.0 | 6.5 | 1847 | 865 | 10122 | 164 | 3470 | 1486 | 11.5 | 0.2 | 4.0 | 3.1 | 7848 | 1767 | 2766 | 44 | 714 |
| M6 | Handpump | 5.0 | 6.9 | 1098 | 987 | 1545 | 1037 | 2897 | 1705 | 10.2 | 0.4 | 13.0 | 16.1 | 2060 | 270 | 479 | 35 | 292 |
| NB-M29 | Handpump | 5.0 | 6.6 | 1200 | 974 | 4319 | 95 | 2070 | 1506 | 10.9 | 0.1 | 0.1 | 0.1 | 3573 | 754 | 1125 | 43 | 406 |
| NB126 | Borewell | 9.5 | 7.2 | 1170 | 1088 | 1286 | 63 | 2336 | 2597 | 9.1 | 3.6 | <dl | 0.2 | 2390 | 225 | 2684 | 47 | 474 |
| NB30 | Borewell | 42.7 | 6.8 | 1796 | 1487 | 1639 | 362 | 4612 | 3932 | 21.3 | 0.5 | <dl | 0.1 | 5325 | 286 | 4928 | 76 | 1033 |
| B162 | Borewell | 9.1 | 7.0 | 1100 | 1119 | 1865 | 52 | 3008 | 1816 | 10.9 | 0.2 | <dl | 0.1 | 1662 | 326 | 1739 | 47 | 320 |
| Stream 1 | Stream | | 7.7 | 1148 | 868 | 2906 | 41 | 1470 | 2856 | 9.3 | 0.2 | 2.5 | 0.1 | 507 | 507 | 711 | 35 | 244 |
| *Wet season* | | | | | | | | | | | | | | | | | | |
| ABW | Piezometer | 6 | 7.6 | 663 | 67 | 2093 | 95 | 358 | 1379 | 1.0 | 0.2 | 0.7 | 0.5 | 512 | 365 | 25 | 16 | 185 |
| ABW2 | Piezometer | 6.8 | 7.1 | 1423 | 958 | 2511 | 21 | 2030 | 3717 | 17.7 | 0.1 | 1.0 | 3.8 | 1858 | 438 | 1147 | 31 | 500 |
| B100 | Borewell | 4.5 | 6.9 | 2050 | 1037 | 12573 | 79 | 2841 | 1415 | 11.8 | 0.3 | 0.0 | 0.1 | 9084 | 2195 | 1751 | 29 | 393 |
| B132 | Borewell | 10 | 6.7 | 2180 | 1002 | 3562 | 151 | 4214 | 6015 | 29.7 | 0.3 | 0.1 | 0.6 | 10492 | 622 | 2195 | 62 | 715 |
| B156 | Borewell | 4 | 7.0 | 1362 | 1040 | 4255 | 66 | 2480 | 2551 | 10.2 | 0.2 | 0.0 | 0.3 | 3391 | 743 | 1747 | 31 | 438 |
| B167 | Borewell | 8 | 7.0 | 1022 | 933 | 1924 | 49 | 2311 | 2260 | 9.1 | 0.2 | 0.1 | 0.2 | 1424 | 336 | 1290 | 28 | 239 |
| B30 | Borewell | 40.8 | 6.3 | 2500 | 1299 | 4687 | 1250 | 6498 | 3537 | 18.5 | 0.2 | 0.1 | 0.4 | 8440 | 818 | 3662 | 51 | 1783 |
| B35 | Piezometer | 36.5 | 6.7 | 934 | 1396 | 2701 | 178 | 1906 | 1759 | 6.8 | 0.2 | 0.1 | 0.2 | 384 | 472 | 631 | 33 | 178 |
| B70 | Borewell | 14.3 | 6.7 | 2750 | 1042 | 11947 | 84 | 5330 | 2457 | 20.9 | 0.2 | 0.1 | 0.7 | 14266 | 2086 | 1133 | 66 | 3305 |
| M29 | Handpump | 5 | 6.9 | 1235 | 672 | 3877 | 291 | 2460 | 1664 | 12.1 | 0.9 | 5.5 | 46.4 | 4947 | 677 | 1 | 28 | 289 |
| M30 | Handpump | 5 | 6.8 | 1808 | 891 | 9913 | 174 | 2977 | 1124 | 17.1 | 0.2 | 0.7 | 16.7 | 7365 | 1731 | 1377 | 41 | 1044 |
| M6 | Handpump | 5 | 6.9 | 984 | 704 | 1451 | 1611 | 2542 | 1557 | 9.7 | 0.2 | 17.6 | 91.2 | 1620 | 253 | 0 | 28 | 212 |
| NB-M29 | Handpump | 5 | 6.9 | 1162 | 891 | 4371 | 90 | 2357 | 1425 | n.a | n.a | n.a | n.a | 3791 | 763 | 773 | 22 | 439 |
| NB126 | Borewell | 10 | 6.8 | 964 | 1010 | 1164 | 49 | 2661 | 2209 | 7.9 | 0.3 | 0.0 | 0.1 | 1963 | 203 | 2143 | 27 | 394 |
| NB30 | Borewell | 40 | 6.7 | 2580 | 1259 | 2666 | 418 | 6824 | 5037 | 27.2 | 0.2 | 0.0 | 0.2 | 10628 | 465 | 8313 | 67 | 2116 |
| B162 | Borewell | 10 | 6.7 | 1116 | 1117 | 1701 | 47 | 3091 | 1896 | n.a | n.a | n.a | n.a | 2115 | 297 | 1979 | 29 | 319 |
| ABW3 | Borewell | 6.5 | 7.5 | 1248 | 893 | 2492 | 28 | 1921 | 3668 | 18.0 | 1.2 | 1.1 | 0.2 | 1905 | 435 | 1167 | 30 | 502 |
| Stream1 | Stream | | 7.5 | 1000 | 597 | 2627 | 95 | 1866 | 1965 | 8.2 | 0.3 | 1.5 | 0.1 | 1576 | 1576 | 350 | 26 | 235 |
| Stream2 | Stream | | 7.2 | 530 | 321 | 2341 | 83 | 883 | 528 | 3.9 | 0.2 | 0.5 | 0.3 | 1702 | 1702 | 13 | 16 | 121 |
| Tank | Monsoon tank | | 7.1 | 262 | 179 | 752 | 113 | 512 | 342 | 2.4 | 0.3 | 0.0 | 0.3 | 440 | 440 | 1 | 13 | 93 |
| Spring | Surface spring | | 6.2 | 72 | 458 | 572 | 7 | 26 | 23 | 0.2 | 1.1 | 0.1 | 0.3 | 153 | 153 | 11 | 12 | 36 |
| **Mule Hole** | | | | | | | | | | | | | | | | | | |
| *Dry season* | | | | | | | | | | | | | | | | | | |
| P1 | Piezometer | 7.6 | 6.3 | 399 | 588 | 310 | 87 | 1397 | 817 | 3.3 | 0.4 | 3.7 | 9.1 | 198 | n.a | 2 | 19 | 26 |
| P10 | Piezometer | 14.1 | 6.6 | 624 | 881 | 1806 | 93 | 1522 | 1004 | 4.8 | 0.2 | 9.9 | 1.7 | 533 | n.a | 1 | 22 | 87 |
| P12 | Piezometer | 10.8 | 6.4 | 467 | 477 | 904 | 121 | 1184 | 863 | 3.4 | 0.2 | 12.3 | 0.8 | 268 | n.a | 1 | 19 | 156 |
| P13 | Piezometer | 9.8 | 6.6 | 400 | 671 | 902 | 116 | 958 | 828 | n.a | n.a | n.a | n.a | 240 | n.a | 1 | 17 | 59 |
| P3 | Piezometer | 22.5 | 6.8 | 806 | 889 | 1360 | 216 | 1981 | 1569 | 5.5 | 0.3 | 7.8 | 24.5 | 745 | n.a | 1 | 32 | 87 |
| P5 | Piezometer | 31.7 | 6.5 | 592 | 759 | 1578 | 181 | 1357 | 1055 | 3.8 | 0.5 | 0.5 | 0.1 | 505 | n.a | 1 | 26 | 74 |
| P6 | Piezometer | 33.6 | 6.8 | 751 | 689 | 1007 | 130 | 1321 | 1658 | 3.2 | 0.4 | 9.9 | 1.6 | 214 | n.a | 1 | 30 | 180 |

(*continued on next page*)

**Table 1** (*continued*)

| | | Depth | pH | Conductivity | DSi | Na | K | Ca | Mg | Sr | Al | Mn | Fe | Cl | Cl# | $NO_3$ | $PO_4$ | $SO_4$ |
|---|---|---|---|---|---|---|---|---|---|---|---|---|---|---|---|---|---|---|
| | | m | | µS/cm | µM | µM | µM | µM | µM | µM | µM | µM | µM | µM | µM | µM | µM | µM |
| P7 | Piezometer | 8.6 | 6.5 | 584 | 868 | 570 | 43 | 1680 | 1363 | 5.7 | 0.2 | 1.6 | 4.6 | 173 | n.a | 2 | 28 | 78 |
| P9 | Piezometer | 13.3 | 6.6 | 702 | 860 | 1852 | 139 | 1809 | 1049 | 5.4 | 0.3 | 13.7 | 19.3 | 602 | n.a | 2 | 29 | 11 |
| Nugu River | River | | 7.2 | 138 | 417 | 391 | 57 | 253 | 252 | 1.1 | 0.2 | 1.7 | 0.9 | 156 | n.a | 5 | 10 | 8 |
| *Wet season* | | | | | | | | | | | | | | | | | | |
| P1 | Piezometer | 1.5 | 5.8 | 172 | 639 | 226 | 39 | 395 | 283 | 1.5 | 0.6 | 0.3 | 0.2 | 87 | n.a | 1 | 14 | 32 |
| P10 | Piezometer | 14.1 | 6.6 | 624 | 886 | 1753 | 94 | 1264 | 877 | 4.5 | 0.9 | 5.3 | 0.7 | 595 | n.a | 1 | 27 | 107 |
| P12 | Piezometer | 9.2 | 6.4 | 467 | 483 | 942 | 118 | 1201 | 921 | 4.2 | 0.9 | 16.7 | 0.5 | 462 | n.a | 1 | 17 | 188 |
| P13 | Piezometer | 8.9 | 6.4 | 452 | 617 | 854 | 122 | 908 | 826 | 2.7 | 1.1 | 6.4 | 0.3 | 230 | n.a | 1 | 19 | 69 |
| P3 | Piezometer | 21.7 | 5.8 | 150 | 410 | 206 | 124 | 352 | 188 | 1.3 | 0.7 | 1.5 | 1.8 | 81 | n.a | 1 | 12 | 16 |
| P5 | Piezometer | 31.9 | 6.2 | 722 | 886 | 1528 | 190 | 1293 | 1050 | 3.8 | 0.3 | 0.0 | 0.1 | 513 | n.a | 1 | 23 | 71 |
| P6 | Piezometer | 34.4 | 6.5 | 910 | 677 | 938 | 125 | 2085 | 1605 | 3.1 | 0.2 | 13.0 | 3.9 | 212 | n.a | 0 | 26 | 150 |
| P7 | Piezometer | 2.4 | 6.3 | 647 | 739 | 522 | 48 | 1755 | 1536 | 6.6 | 0.8 | 0.2 | 0.2 | 123 | n.a | 0 | 24 | 156 |
| P9 | Piezometer | 13.2 | 6.1 | 485 | 776 | 1080 | 112 | 1199 | 691 | 4.3 | 0.8 | 8.1 | 4.2 | 373 | n.a | 1 | 20 | 120 |
| Nugu River | River | | 6.2 | 107 | 256 | 264 | 68 | 203 | 137 | 0.9 | 0.3 | 0.0 | 0.4 | 206 | n.a | 37 | 11 | 20 |
| MH Stream | Stream | | 6.9 | 169 | 453 | 487 | 119 | 340 | 232 | 1.2 | 1.4 | 0.1 | 0.5 | 225 | n.a | 1 | 13 | 7 |
| Stream 3 | Stream | | na | n.a | 299 | 858 | 77 | 401 | 290 | 1.1 | 1.2 | 0.1 | 0.6 | 313 | n.a | 0 | 14 | 21 |

**Table 2**
The isotope ratios of H, O, Sr and Si from Berambadi and Mule Hole during the dry and wet season. The '*' denotes the standard deviation of chemically triplicated samples and the rest is only duplicated and denote variability.

| | $\delta^{18}O$ | $\delta^{2}H$ | $\delta^{30}Si$ | 1SD |
|---|---|---|---|---|
| | ‰ | ‰ | ‰ | ‰ |
| **Berambadi** | | | | |
| *Dry season* | | | | |
| ABW | −3.8 | −21.6 | 2.96 | 0.04 |
| ABW2 | −2.9 | −17.7 | 1.13 | 0.13* |
| B100 | −2.6 | −13.1 | 0.68 | 0.06* |
| B132 | −3 | −18.6 | 0.97 | 0.02 |
| B156 | −3.2 | −18.4 | 0.74 | 0.08 |
| B167 | −3.5 | −20.6 | 1.10 | 0.14 |
| B30 | −2.6 | −14.2 | 0.76 | 0.09 |
| B35 | −3.4 | −19.5 | 1.06 | 0.03 |
| B70 | −1.7 | −10.8 | 0.93 | 0.05 |
| M29 | −3 | −16.2 | 1.49 | 0.10* |
| M30 | −2.4 | −12.5 | 1.48 | 0.10* |
| M6 | −2.4 | −11.8 | 0.69 | 0.08* |
| NB-M29 | −2 | −9.8 | 1.02 | 0.11* |
| NB126 | −3.2 | −19 | 1.02 | 0.13* |
| NB30 | −3.2 | −18.1 | 0.63 | 0.05 |
| B162 | −3.5 | −21.1 | 0.84 | 0.08 |
| Stream 1 | −3.4 | −19.6 | 1.64 | 0.04 |
| *Wet season* | | | | |
| ABW | −3.8 | −19.7 | 3.45 | 0.01 |
| ABW2 | −3.1 | −17.7 | 1.41 | 0.10* |
| B100 | −2.7 | −12.7 | 0.88 | 0.04 |
| B132 | −3.4 | −19.8 | 0.70 | 0.12* |
| B156 | −3.4 | −18.8 | 0.59 | 0.06 |
| B167 | −3.6 | −20.8 | 1.20 | 0.08* |
| B30 | −2.2 | −9.6 | 0.83 | 0.05 |
| B35 | −3.5 | −19 | 0.89 | 0.10* |
| B70 | −1.8 | −8.9 | 1.08 | 0.09* |
| M29 | −3.2 | −16 | 1.82 | 0.11* |
| M30 | −3 | −13 | 1.59 | 0.12* |
| M6 | −2.7 | −12.4 | 1.44 | 0.07 |
| NB-M29 | −1.9 | −9.3 | 0.75 | 0.02 |
| NB126 | −3.3 | −19.1 | 0.85 | 0.08 |
| NB30 | −2.6 | −14.9 | 0.80 | 0.02 |
| B162 | −3.5 | −20.4 | 0.90 | 0.10* |
| ABW3 | −3.1 | −17.6 | 1.20 | 0.04 |
| Stream1 | −3.1 | −16.1 | 1.78 | 0.15 |
| Stream2 | −2.5 | −10.5 | 1.89 | 0.08* |
| Tank | −2.3 | −10.1 | 1.60 | 0.06 |
| Spring | −3.1 | −12.8 | 0.97 | 0.06 |
| | | | | |
| **Mule Hole** | | | | |
| *Dry season* | | | | |
| P1 | −2.4 | −6.8 | 1.47 | 0.15 |
| P10 | −3.3 | −14.8 | 1.06 | 0.02 |
| P12 | −2.5 | −9.2 | 1.07 | 0.18* |
| P13 | −2.9 | −12.9 | 1.14 | 0.13 |
| P3 | −3.4 | −16.4 | 0.59 | 0.11 |
| P5 | −3.6 | −16.7 | 0.97 | 0.12 |
| P6 | −2.8 | −16.9 | 0.85 | 0.1 |
| P7 | −2.7 | −9.4 | 1.23 | 0.10* |
| P9 | −3.6 | −17 | 1.03 | 0.03 |
| Nugu River | −1.8 | −6.9 | 2.19 | 0.09* |
| *Wet season* | | | | |
| P1 | −2.2 | −4.9 | 1.31 | 0.13 |
| P10 | −3.3 | −14.1 | 0.88 | 0.04 |
| P12 | −1.7 | −2.1 | 0.97 | 0.04 |
| P13 | −3.3 | −13.8 | 0.75 | 0.03 |
| P3 | −3.2 | −13.8 | 0.93 | 0.07 |
| P5 | −3.7 | −17 | 0.65 | 0.06 |
| P6 | −3.3 | −18.1 | 0.60 | 0.01 |
| P7 | −2.5 | −6.4 | 1.09 | 0.09* |
| P9 | −2.7 | −8.3 | 1.08 | 0.01 |
| Nugu River | −2.8 | −10.1 | 1.47 | 0.08* |
| MH Stream | −2.5 | −7.9 | 1.52 | 0.06 |
| Stream 3 | −2.1 | −6.3 | 1.51 | 0.11 |
| Diatomite | – | – | 1.19 | 0.09 (1 SD, n = 100) |

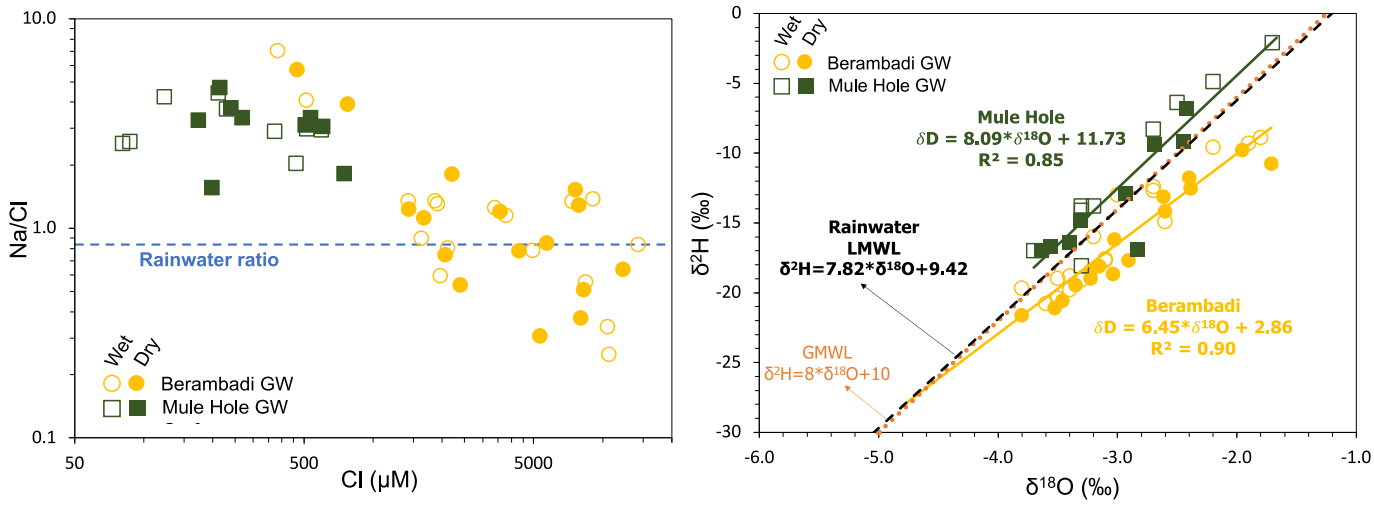


**Fig. 2.** The plot depicting, *a)* Na/Cl and Cl of groundwater, showing increasing Cl concentration and a concurrent reduction in Na/Cl ratio below the rainwater ratio of 0.81 (dashed line, Riotte et al., 2014a), *b)* $\delta^{18}O$ and $\delta^{2}H$ bivariate plots for groundwater from Mule Hole and Berambadi along with the local meteoric water line (LMWL, black dashed line, Table S2) from local precipitation and global meteoric water line (GMWL, orange dashed line, Craig (1961)). Equations for the linear relationship between $\delta^{18}O$ and $\delta^{2}H$ for all groundwater from watershed across both season is shown.

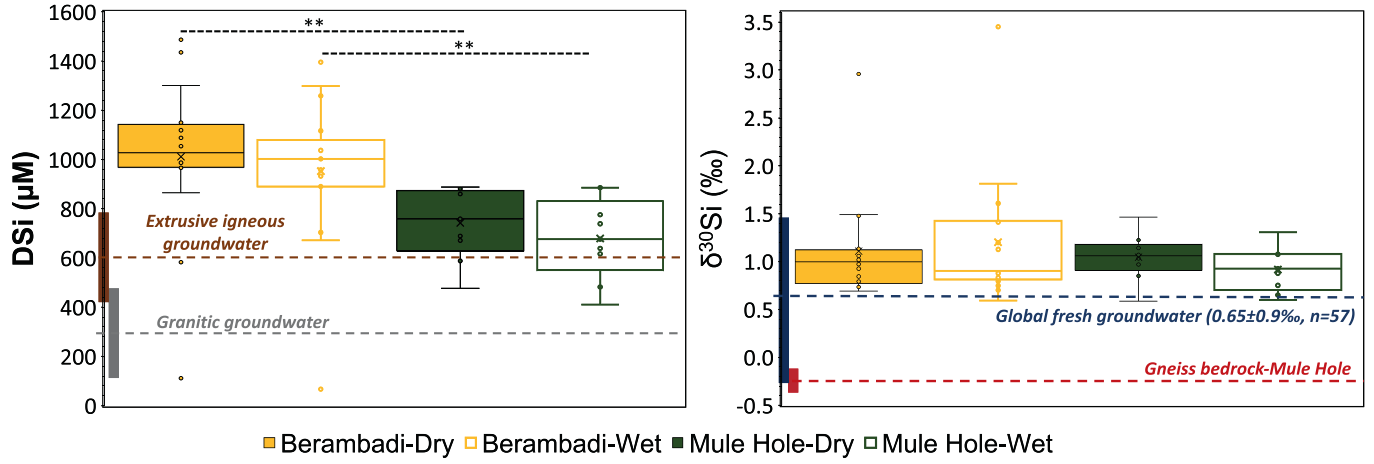


**Fig. 3.** Box plot showing the variability of a) dissolved silicon (DSi), b) silicon isotopic composition of groundwater from the present study. The horizontal dashed lines represent the average of the published DSi values of similar aquifer lithology globally (Rahman et al., 2019) and $\delta^{30}Si$ (Frings et al., 2016; Ehlert et al., 2016; Martin et al., 2021) with parent gneiss $\delta^{30}Si$ in Mule Hole published by Riotte et al. (2018a). The thick bars region represents ±1SD variability of published average values and the black dashed lines denotes significant differences (** implies level of significance with *p-value* < 0.01).

groundwater from Berambadi (1.2 ± 0.6 ‰, $n = 33$) and Mule Hole (1.0 ± 0.2 ‰, $n = 18$) exhibits comparable $\delta^{30}Si$ values, in the higher side of present global groundwater average of 0.5 ± 0.9 ‰ ($n = 66$) (Fig. 3, Ziegler et al., 2005; Georg et al., 2009a, 2009b; Opfergelt et al., 2013; Pokrovsky et al., 2013; Pogge von Strandmann et al., 2014; Ehlert et al., 2016; Riotte et al., 2018a; Martin et al., 2021). Interestingly, shallow groundwater (<10 m) exhibited a larger variability in $\delta^{30}Si$ (1.3 ± 0.6 ‰, $n = 28$) compared to the deeper groundwater (0.9 ± 0.2 ‰, $n = 23$). We did not observe any significant differences in $\delta^{30}Si$ values of groundwater between dry and wet season from groundwater within each watershed (Fig. 3b). A significant negative correlation was found between DSi and $\delta^{30}Si$, with heavier $\delta^{30}Si$ corresponding to a loss of DSi from the system ($R^2 = 0.42$, $p$ value<0.05, Fig. 4a).

The $\delta^{30}Si$ values of surface water samples collected from small streams close to the groundwater samples and of Nugu river showed an average value of 1.7 ± 0.5 ‰, which was significantly heavier than the overall groundwater (*p-value* < 0.01, Table 2). The measured DSi in soil solution from Berambadi ranges from 370 μM to 715 μM (590 ± 120 μM, $n = 8$), with an average $\delta^{30}Si$ value of 1.5 ± 0.3 ‰ (1SD, n = 8), significantly higher in $\delta^{30}Si$ composition compared to groundwater from the watershed (*p-value* < 0.001). Previously published isotopic data of bedrock, clay, rainwater, and soil solution from Mule Hole watershed are compiled in Table 3.

## 4. Discussion

Based on the watershed level $\delta^{30}Si$ signatures of the surface, soil, and groundwater hydrologic compartments, two major inferences can be reached. First, groundwater $\delta^{30}Si$ values (1.1 ± 0.5 ‰, $n = 51$) are significantly lower than the soil solutions (1.6 ± 0.2 ‰, $n = 17$ present study and Riotte et al., 2018a) and river systems from South India (1.4 ± 0.7 ‰, $n = 46$, Sarath et al., 2022), hinting towards a differential control on silicon isotopic composition in groundwater compared to surface compartments (*p-value* < 0.01, Fig. 4, Fig. S2). Secondly, we found no significant seasonal, nor landuse based differences in groundwater $\delta^{30}Si$ composition for both the Mule Hole and Berambadi watershed, indicating a significant buffer to spatio-temporal variability of $\delta^{30}Si$ in groundwater systems (Fig. 3). In the following sections we

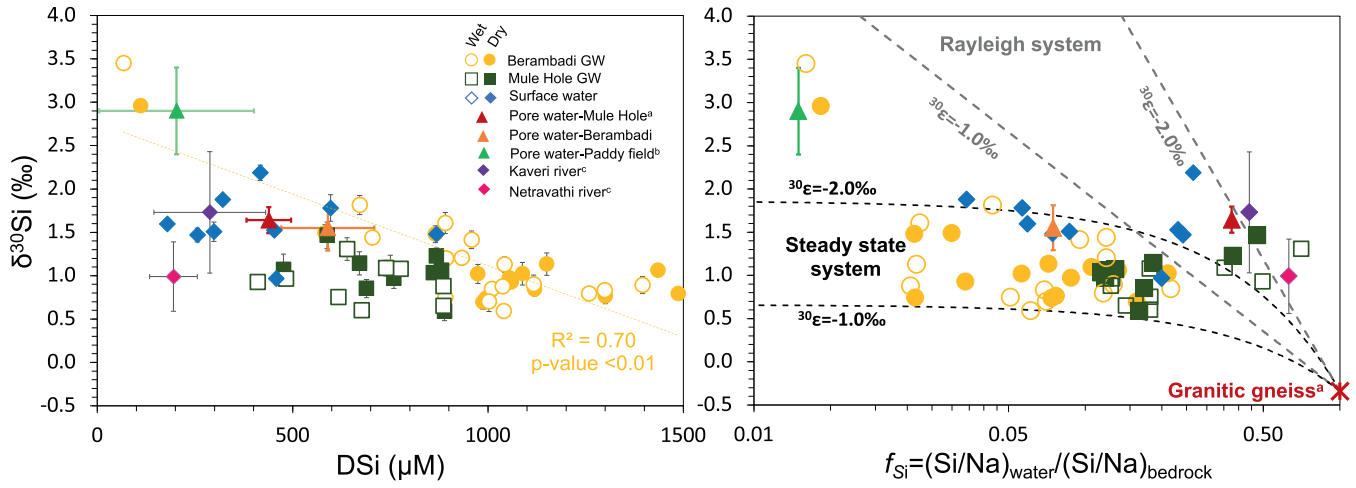


**Fig. 4.** The plot between δ $^{30}$Si and a) dissolved silicon in groundwater and surface water from Mule Hole and Berambadi, (the error bar indicates 1SD), the regression line has been shown for Berambadi groundwater, b) Evolution of $\delta^{30}$Si with fraction of Si mobilized into dissolved phase ($f_{Si}$) during weathering (see section 2.5.2 for more details). Dashed and dotted lines represent the evolution of $\delta^{30}$Si expected from Si removal under two model scenarios: i) Rayleigh distillation from a finite Si pool, ii) steady-state open flow through model (Bouchez et al., 2013) (a: Riotte et al. (2018a), b: Riotte et al. (2018b), c: Sarath et al. (2022)).

**Table 3**
The Si isotope ratio of various endmembers from the present study and Riotte et al. (2018a), both from the same region.

| Compartments | Location | $\delta^{30}$Si | Reference |
|---|---|---|---|
| | | ‰ | |
| Granitic gneiss | Mule Hole | −0.34 ± 0.08 (1SD, n = 3) | Riotte et al., 2018a |
| Soil pore water | Berambadi | 1.55 ± 0.26 (1SD, n = 8) | Present study |
| | Mule Hole | 1.64 ± 0.15 (1SD, n = 9) | Riotte et al., 2018a |
| Clay fraction | Mule Hole | −1.3 ± 0.03 (1SD, n = 3) | Riotte et al., 2018a |

discuss the major processes controlling the groundwater composition and Si dynamics in the two watersheds.

### 4.1. Main drivers of groundwater chemical composition

Groundwater in the Berambadi watershed exhibits high solute concentration compared to Mule Hole, resulting from multiple pumping/return flow cycles induced by the widespread groundwater irrigation in Berambadi. This agricultural practice leads to enhanced relative evapotranspiration in Berambadi, while solutes like $Cl^-$ and $NO_3^-$ also result from the excessive fertilizer application (Table 1, Fig. 2, Fig. S1). In a plot of $Na^+/Cl^-$ versus $Cl^-$ concentration, the Berambadi samples exhibit a negative correlation, with $Na^+/Cl^-$ ratio often lower than the local rainwater value of ~0.81 (Fig. 2, Riotte et al., 2014), resulting from $Cl^-$ inputs through fertilization with potash. The evaporation component of evapotranspiration process was assessed from $\delta^2$H and $\delta^{18}$O isotopic compositions of groundwater; evaporation enriches residual water in heavy isotopes of H and O, while biological processes such as transpiration does not fractionate water isotopes (Good et al., 2015; Evaristo et al., 2015). Indeed, groundwater samples from Mule Hole plot close to the local meteoric water line (LMWL) with a similar slope in the $\delta^2$H vs. $\delta^{18}$O plot, indicating the absence of detectable evaporation in the forested watershed (Fig. 2). The Berambadi groundwater exhibits significant deviation to the right of LMWL with a low deuterium excess (d-excess) values and a negative correlation between d-excess and conductivity (Fig. 2, S1). Using Gonfiantini (1986) approach at an ambient relative humidity of 84 % and air temperature of 25 °C, estimated evaporative loss in Berambadi groundwater would be on average 22 % (Clark, 2015; Riotte et al., 2021a, 2021b). In Mule Hole, with an average rainfall of 1200 mm/year, the evapotranspiration by deep rooted trees during the percolation dominates the water cycling, even leading to the disconnection of groundwater with the surface runoff (Maréchal et al., 2009; Ruiz et al., 2010). A significant lag in groundwater table response to the precipitation events is also observed in the watershed, indicating that water transit through the regolith is long, up to 20 years according to the COMFORT model (Riotte et al., 2014). In the Berambadi watershed, despite a lower annual rainfall of 800 mm/yr, the recharge flux to the groundwater is enhanced by irrigation and return flow (irrigated water not taken up by plants or evaporated), which may in turn shorten the transit time in the regolith of the watershed. The succession of pumping/return flow cycles explains the evaporative enrichment, degradation of groundwater quality in the Berambadi watershed, often associated nitrate hotspots. This is also enhanced by the small hydraulic gradient and limited lateral groundwater flow in the watershed (Buvaneshwari et al., 2017). We can infer that the higher DSi of groundwater in Berambadi compared to Mule Hole during both seasons can be attributed to the combined effect of physical processes such as evaporation and transpiration, arising due to groundwater recycling from pumping and irrigation in the cultivated watershed. However, we do not observe any significant impact on Si isotopic composition of groundwater through the enrichment process.

### 4.2. Silicate weathering controls on δ $^{30}$Si of groundwater

The dissolved silicon in terrestrial watersheds primarily originates from silicate weathering, which includes both dissolution of primary silicate minerals and formation of secondary clays in the weathering profile. The majority of the regolith Si pool in both watersheds is still composed of primary minerals (86–95 %, principally quartz) with a small proportion of kaolinite and smectites (4–13 %; Braun et al., 2009, Riotte et al., 2018a). Before entering the saturated part of the aquifer, the DSi and $\delta^{30}$Si signatures of percolating water are affected by slow processes such as clay mineral precipitation and/or crystal growth, as well as relatively fast processes such as adsorption onto oxy-hydroxides and biotic uptake (Frings et al., 2016 and the references therein). The incongruent weathering of silicate minerals is evident in both watersheds, with heavier groundwater $\delta^{30}$Si value in both Berambadi and Mule Hole compared to the parent gneiss bedrock values of −0.34 ± 0.08 ‰ reported previously (Fig. 3; Riotte et al., 2018a). Based on the assumption and normalization procedure detailed in Section 2.4, we estimate that on average 91 % and 76 % of the Si mobilized from the parent gneiss in Berambadi and Mule Hole watersheds, respectively, is incorporated into secondary phases, resulting in $\delta^{30}$Si of groundwater with positive values ranging from 0.6 ‰ to 3.4 ‰ (Table 1). A similarly low $f_{Si}$ was also reported for a compilation of stream waters by

Fernandez et al. (2022), where distinct $\delta^{30}Si$ signatures observed in stream water was linked to multiple fractionating pathways and hydrologic routing. In Berambadi, we observe a negative correlation between DSi and $\delta^{30}Si$ value of groundwater ($r^2 = 0.69$), indicating Si loss and subsequent fractionation favoring heavier isotopes in the residual waters, while no such relationship exists in Mule Hole (Fig. 4a). Given that absolute concentration can be affected by dilution and evapotranspiration, we use $f_{Si}$ to further interpret the fractionation processes and pathways. The observed higher DSi and lower $f_{Si}$ in Berambadi groundwater indicates higher proportion of Si is immobilized into secondary phases as the recycled groundwater moves through soil and saprolite layers (Fig. 4b). A majority of groundwater samples from both watersheds indeed fit a steady-state system with a slope, i.e. isotopic fractionation ($^{30}\varepsilon$), between −1.0 ‰ and − 2.0 ‰ (Fig. 4b; see Eq. 5, Riotte et al., 2018a, 2018b, Frings et al., 2021).

Three scenarios may explain the observed linear dependency in groundwater Si isotope evolution: *a)* the whole weathering zone acts as a homogenous reactor at steady-state, where a dynamic equilibrium balances the silicon supply to groundwater and the Si removal through precipitation of the secondary phases in soil and saprolite (Bouchez et al., 2013), *b)* a continuous exchange between the precipitating solids and coevolving solution (Fernandez et al., 2019), and *c)* the mixing of fluids from multiple flow-paths characterized by exponential distribution of travel times, each following a Rayleigh model (Druhan and Maher, 2017). The scenario *a* is indeed logical with our current knowledge of the water cycle in the region. In hard-rock aquifers, groundwater recharge is spatially distributed and occurs by percolation through a thick regolith, which steadily supplies Si from silicate-weathering reactions, themselves balanced by the formation of secondary clays. An independent estimate of the fractionation factor ($^{30}\varepsilon$) between dominant kaolinite and bedrock in Mule Hole watershed is close to −1 ‰, consistent with the lower limit of modelled $^{30}\varepsilon$, supporting scenario *a* (Riotte et al., 2018a). Unlike surface water systems, where we expect no interaction between precipitated solids and the solution as the water rapidly leaves the weathering profile, slow percolation of soil solution through porous immature saprolite might be more favorable to isotopic re-equilibration with secondary phases, as described in scenario *b*. The extent of re-equilibration should depend on the surface area and mass of the precipitated phase, which is a function of the regolith thickness and the depth to which the fluid can interact within mineral surfaces and can occur within timescales of few weeks (Fernandez et al., 2019; Zheng et al., 2019). However, continuous isotopic exchange (scenario *b*) is difficult to attain in open systems like a weathering profile and cannot explain the observed $\delta^{30}Si$ from the region due to two compelling reasons. First, according to ab initio calculations, the estimated equilibrium fractionation factor between kaolinite and $H_4SiO_4$ is +0.4 ± 0.2 ‰ (Dupuis et al., 2015), which would make the clay fraction $\delta^{30}Si$ heavier than the bedrock (−0.3 ‰) or soil porewater (1.6 ‰) values (Riotte et al., 2018a). The $\delta^{30}Si$ of the clay fraction from Mule Hole (predominantly kaolinite) is −1.3 ± 0.03 ‰, which indicates no significant re-equilibration (Riotte et al., 2018a). We must be cautious here while comparing present-day water with clay minerals composition, given that clay minerals integrate signatures over long timescales with possibly different pedoclimatic conditions, while soil porewater signatures only reflects present-day water-rock interactions. Additionally, re-equilibration is an exchange process, which cannot account for the DSi increase between soil porewater and groundwater as observed in both watersheds. In a simple Rayleigh distillation model (Eq. 4), the isotopic fractionation can arise from a fast-unidirectional uptake of Si into secondary minerals and amorphous phases. It is observed only in few Mule Hole groundwaters, soil solutions and surface waters (including streams and major rivers) (Fig. 4b, Geilert et al., 2014; Oelze et al., 2015). Deviation from the simple Rayleigh model can occur in groundwaters, which acquire $\delta^{30}Si$ signatures through mixing of fluids from multiple flow paths and/or fractures with variable travel times (Druhan and Maher, 2017). A revised Rayleigh model can also be applied for fluids with fractionating first order kinetic reactions and an exponential travel time distribution, giving an expression functionally similar to Eq. 5, as described in scenario *c* (Druhan and Maher, 2017). Such a framework with non-uniform travel time distributions has been successfully applied to explain the $\delta^{30}Si$ variability in different stream watersheds across the globe (Fernandez et al., 2022). However, scenario *c* is difficult interpret in the studied watersheds without better constraints for travel time distributions and flow paths characteristics, especially in Berambadi with irrigated agriculture. In the next two sections we explore the possible Si sources and fractionation pathways in shallow surface/subsurface layers and deep weathering zones and how they alter the Si isotopic composition of groundwater.

### 4.3. Shallow surface and subsurface processes

Groundwater recharge can be distributed over the surface area of the watershed (so-called "direct") and/or occur in discrete zones, for instance by infiltration through the streambed (so-called "indirect") (Maréchal et al., 2009). During direct recharge, the $\delta^{30}Si$ signatures of soil porewaters are first affected by water-soil-plant interactions before being transferred to shallow groundwater systems. Previous work from temperate settings have shown that the $\delta^{30}Si$ values of soil porewater was significantly heavier in old cropland compared to forested landscapes, owing to the long-term crop removal and subsequent reduction in soil biogenic Si (BSi) (Delvaux et al., 2013; Vandevenne et al., 2015). Within Indian subcontinent, soil porewater from diverse landuse settings exhibit heterogeneous $f_{Si}$ and $\delta^{30}Si$ composition (Fig. 4b, Riotte et al., 2018a, 2018b). The most extreme isotopic fractionation occurs in soil porewater from paddy field, with a high $\delta^{30}Si$ (2.9 ± 0.4 ‰) and a low DSi (214 ± 196 μM). These porewaters are shown to follow a Rayleigh model type behavior, resulting from significant Si uptake by rice crop and adsorption processes occurring at the ground surface of the paddy and within the soil (Riotte et al., 2018b). In Berambadi, soil porewaters exhibit a lower $\delta^{30}Si$ and a steady-state model, consistent with the input of recycled groundwater by irrigation, and the absence of Si-accumulating crops in the sampling area (common crops include cabbage and garlic) (Fig. 4b). On the other hand, soil porewater from Mule Hole follows a Rayleigh model with high $f_{Si}$ but similar $\delta^{30}Si$ to Berambadi, which was previously assigned to plant uptake by deciduous trees and/or adsorption processes in addition to Na-plagioclase weathering in the upper soil (Riotte et al., 2018a).

The shallow groundwater (<10 m) composition can be influenced by infiltrating soil porewater through preferential flow paths and local recharge processes, inheriting signatures of soil processes (Sprenger et al., 2019). In both Mule Hole and Berambadi, $\delta^{30}Si$ of shallow groundwaters are more heterogenous, ranging from 0.6 to 3.5 ‰, and on average + 0.4 ‰ heavier than deep groundwater, indicating mixing of multiple water sources exhibiting distinct $\delta^{30}Si$ signatures (Fig. 5). As an example, the two hyporheic piezometers P1 and P7 from Mule Hole watershed, both following a Rayleigh behavior, consistent with infiltration of stream water from the streambed during flow periods (Fig. 4b, Maréchal et al., 2009). The stream water $\delta^{30}Si$ signature of 1.5 ‰ in Mule Hole primarily arises from dissolution of amorphous silica from forest-litter decay (Riotte et al., 2018a). Similarly, in Berambadi watershed, a shallow abandoned borewell (ABW, with groundwater table depth of ~6 m) in a maize field exhibit both the highest $\delta^{30}Si$ and the lowest DSi concentration during both seasons, fitting a Rayleigh fractionation line. Such consistent and high $\delta^{30}Si$ values could be indicative of infiltration of soil porewater inherited from plant uptake, comparable to $\delta^{30}Si$ of soil solution from paddy fields in the region (Fig. 4, Riotte et al., 2018b). We can estimate the fractionation factor ($^{30}\varepsilon_{plant\text{-}solution}$) for plant uptake assuming that groundwater composition results from large DSi uptake from shallow soil solution ($DSi_{soil\ solution}$). The fraction of Si remaining in ABW ($f_{Si(ABW)}$) following the plant uptake can be estimated by as:

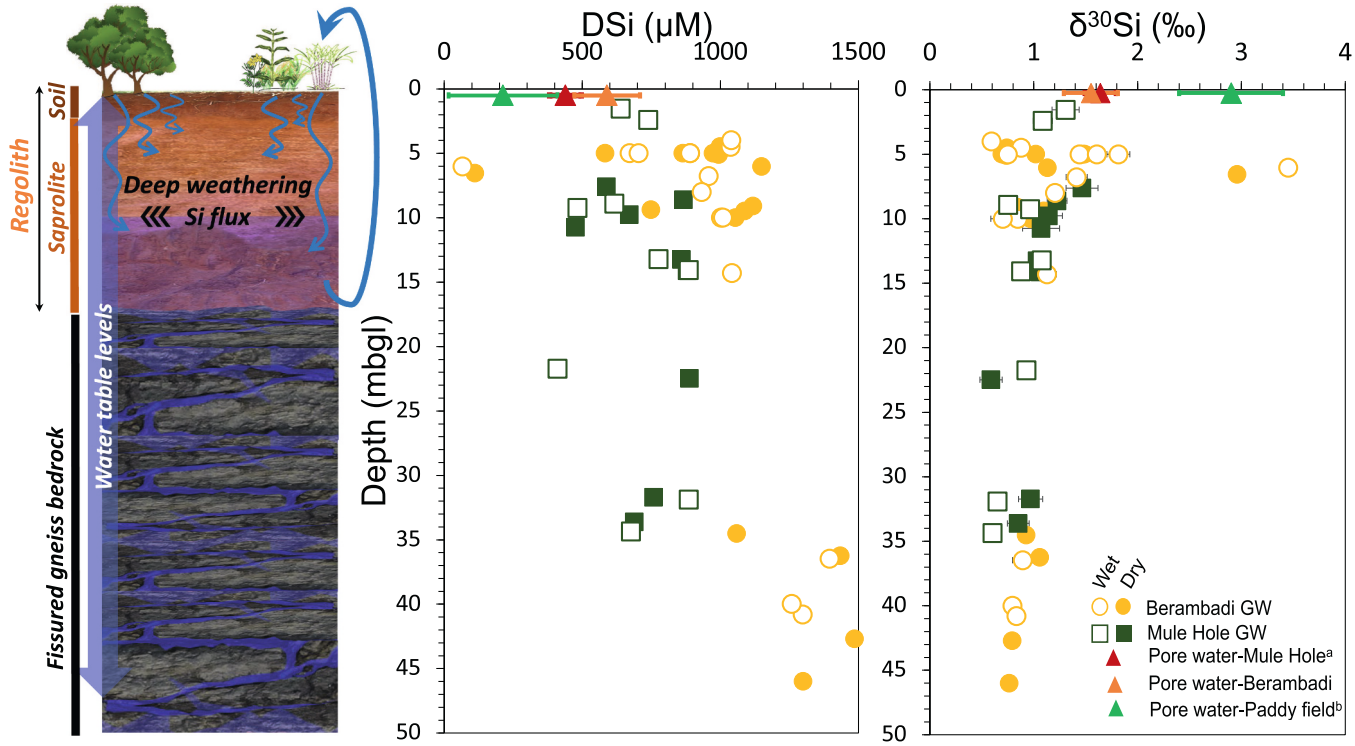


**Fig. 5.** The plot of groundwater water table depth (in meters below ground level or mbgl) vs. $\delta^{30}$Si and DSi in groundwater from Mule Hole and Berambadi collected from different depths. Also plotted soil porewater values from Riotte et al. (2018a), (2018b) (assumed average depth of 1 m). A schematic of the weathering profile typical for the region is given on the left side (Braun et al., 2009).

$$f_{Si(ABW)} = \mathrm{DSi_{ABW}} \Big/ \mathrm{DSi_{soil\ solution}} \quad (6)$$

The calculation assumes that the entire DSi loss in ABW groundwater compared to soil solution is resulting from plant uptake. The $f_{Si(ABW)}$ ranges from 0.19 during dry season and 0.10 during wet season, meaning almost 80–90 % of DSi in groundwater ABW has been lost through plant uptake. Assuming plant uptake follows a Rayleigh fractionation model and applying equation Eq. 4, the $^{30}\varepsilon_{\mathrm{plant\text{-}solution}}$ value ranges between −0.8 ‰ for the dry season and − 0.9 ‰ for the wet season, which lies within the reported silicon isotopic fractionation factors for plant uptake (Sun et al., 2017; Frick et al., 2020; Frings et al., 2021). The isotopic signature of ABW is consistent with the poor connection of this borewell with the local fracture network, limiting the lateral flow and mixing of other water masses in the aquifer and leading to low yield.

Interestingly, the groundwater $\delta^{30}$Si values (1.1 ± 0.5 ‰, $n = 51$) are also significantly lower than the soil pore water (1.6 ± 0.2 ‰, $n = 17$) and river water from South India (1.5 ± 0.7 ‰, $n = 46$), both typically following a Rayleigh system and/or intermediate behavior (Riotte et al., 2018a; Sarath et al., 2022). Similarly to soil porewater in Mule Hole, two major river systems from the study region, the Kaveri and Netravathi rivers, also follow a Rayleigh model integrating Si isotopic signatures of various flow paths in the basin (Sarath et al., 2022). Thus, riverine/stream water $\delta^{30}$Si can be considered as a binary mixture of signatures from: *i)* shallow soil porewater and/or groundwater, which represent signatures of relatively fast near surface processes (e.g. plant uptake), *ii)* deeper groundwaters, which have acquired further signatures of processes occurring in thick regolith layers (Steinhoefel et al., 2017; Stewart et al., 2022). Previous works have attributed the low, and sometimes negative $\delta^{30}$Si values observed in deep groundwater to the dissolution of clay minerals and silcretes (Georg et al., 2009a, 2009b; Pogge von Strandmann et al., 2014). However, this is unlikely the case for Mule Hole and Berambadi watersheds given that the regolith is immature and have high abundance of primary cation-bearing mineral phases. Inaddition, no silcrete has been observed in the weathering profile (Braun et al., 2009; Riotte et al., 2014; Riotte et al., 2018a). Finally, the saturation index calculation using PHREEQC program (*phreeqc.dat* thermodynamic datafile) shows that groundwaters are oversaturated with kaolinite and smectite clays, and undersaturated with abundant primary phases such as albite and chlorite (Fig. S3).

### 4.4. Deep regolith weathering

The $\delta^{30}$Si values of deep groundwater (≥10 m) in both watersheds were homogenous and low (0.9 ± 0.2 ‰, $n = 23$), with higher DSi concentration compared to shallow groundwaters and soil porewaters, indicating an additional source of isotopically light Si (Fig. 5). Considering an average regolith thickness of 17 m in the basin, during the recharge process the deep groundwater will interact with highly porous regolith layers, and underlying fractured gneiss bedrock (Dewandel et al., 2006; Braun et al., 2009). In the Mule Hole watershed, the thick regolith constitutes a major water stock for deep-rooted trees, thus can alter the $\delta^{30}$Si composition of deep groundwater through root uptake (Ruiz et al., 2010; Chitra-Tarak et al., 2018). However, plant uptake cannot explain the observed low groundwater $\delta^{30}$Si values compared to soil porewater, since plants preferentially take up light silicon isotopes, leaving Si-depleted residual solution with high $\delta^{30}$Si values. Moreover, in the cultivated watershed the uptake depths of most short-cycle crops do not exceed 1 m (Robert et al., 2017). A similar argument also holds true for adsorption processes, where adsorption onto Fe oxyhydroxides is also shown to enrich the residual solution in heavy isotopes, which is not the case here (Delstanche et al., 2009). We infer that even if deep DSi uptake by plants and adsorption processes can occur within the regolith layer, it is limited and masked by the release of additional DSi from water-rock interactions. For deep groundwater recharge, the water pass through porous regolith layers with high partial pressure of $CO_2$ and abundant primary minerals, promoting additional weathering reactions which can release Si into solution (Violette et al., 2010). The potential

sources of DSi are primary silicate minerals within the saprolite, which includes quartz (31 %), plagioclase (33 %), biotite (2 %), chlorite (7 %), hornblende (5 %) and sericite (13 %) (Braun et al., 2009; Violette et al., 2010). Quartz and sericite are extremely resistant to weathering and are unlikely to contribute significantly. The majority of DSi supply to groundwater results from the weathering of Na-plagioclase, biotite and chlorite with formation of secondary clays such as kaolinites and smectites, respectively (~3 % volumetric content in saprolite for both clays, Violette et al., 2010). The stoichiometry of mineral weathering reaction for Na-plagioclase and biotite in the deep regolith layers are given as following (Riotte et al., 2018a; Violette et al., 2010):

$$2^{*}Na_{0.92}Ca_{0.08}Al_{1.07}Si_{2.93}O_8\ (Na-plagioclase) + 2H^+ + 9H_2O \rightarrow 1.07Si_2Al_2O_5(OH)_4\ (Kaolinite) + 1.84Na^+ + 0.16Ca^{2+} + 3.72H_4SiO_4 \quad (7)$$

$$1.67^{*}KMg_{1.5}Fe_{1.5}AlSi_3O_{10}(OH)_2\ (Biotite) + 3.2H^+ + 3.5H_2O \rightarrow Si_4O_{10}(OH)_2Mg_{0.33}Al_{1.67}Mg_{0.165}\ (Smectites) + 2.3\ Mg^{2+} + 1.67\ K^+ + 2.5Fe(OH)_3 + 1.0\ H_4SiO_4 \quad (8)$$

This interpretation is also in accordance with observed steady-state model behavior proposed by Bouchez et al. (2013), as the release of silicon through weathering reactions can supply DSi throughout the weathering profile (Fig. 4b). The secondary clay formed in the saprolite can be accumulated in mineral surfaces, as clay infillings and also coatings (Santos et al., 2018). The $\delta^{30}Si$ values of DSi released by weathering of plagioclase/biotite and formation of kaolinite/smectite, can be deduced by mass balance (Bouchez et al., 2013);

$$\delta^{30}Si_{released} = \left(\delta^{30}Si_{prim.sili.} \times f_{Si\ prim.sili.} - \delta^{30}Si_{clay} \times f_{Si\ clay}\right) \Big/ \left(1 - f_{Si\ clay}\right) \quad (9)$$

In Eq. 9, the terms $f_{Si\ prim.\ sili.}$ and $\delta^{30}Si_{prim.\ sili.}$ Denote the fraction of silicon released by primary silicate weathering and the corresponding silicon isotopic composition of the silicate bedrock, while $f_{Si\ clay}$ and $\delta^{30}Si_{clay}$ denote the fraction of silicon incorporated into clay and the silicon isotopic composition of the clays. Here, we assume the entire Si is sourced from weathering of primary silicates (i.e. $f_{Si\ prim.\ sili.} = 1$) and the Si isotopic composition of primary silicate minerals ($\delta^{30}Si_{prim.\ sili.}$) is similar to that of the whole gneissic bedrock (−0.34 ± 0.08 ‰, Riotte et al., 2018a). The $\delta^{30}Si_{clay}$ in kaolinite dominated soil layers of Mule Hole is known (−1.3 ± 0.03 ‰; Riotte et al., 2018a) and $\delta^{30}Si_{clay}$ of smectites is not available for the study region such that we opted for the average published $\delta^{30}Si$ of −0.5 ± 0.4 ‰ (Georg et al., 2009a, 2009b; Opfergelt et al., 2012; Frings et al., 2021). We assign the $f_{Si\ clay}$ values based on the reaction stoichiometry of dominant weathering reactions in the regolith (Eqs. 7, 8). The estimated $\delta^{30}Si_{released}$ of the DSi produced by plagioclase and biotite weathering is 0.21 ‰ and 0.34 ‰, respectively (Table S3). From these signatures, we can estimate the fraction of Si potentially released from deep weathering ($f_{Si\ released}$) of each primary mineral phases to groundwater DSi again from an isotopic balance:

$$f_{Si\ released} \times \delta^{30}Si_{released} + \left(1 - f_{Si\ released}\right) \times \delta^{30}Si_{soilwater} = \delta^{30}Si_{groundwater} \quad (10)$$

In Mule Hole, if the $\delta^{30}Si_{groundwater}$ of 1.0 ± 0.2 ‰ results from a mixing between an infiltrating soil solution at 1.6 ± 0.1 ‰ ($n = 9$, Riotte et al., 2018a) and DSi released from primary silicate weathering, then the deep regolith weathering would contribute from 46 ± 36 to 51 ± 56 % of the groundwater DSi (Table S3). As any deep Si root-uptake by deciduous trees should be balanced by an increase of this weathering flux, this range should be considered as a minimum contribution to groundwater DSi. Similar calculations for Berambadi, based on measured soil porewater $\delta^{30}Si$ of 1.5 ± 0.2 ‰ ($n = 8$), provides a rough estimation of Si contribution from deep weathering fluxes ranging from 34 ± 39 to 38 ± 56 % (Table S3). However, the calculation in Berambadi is complicated by the fact that groundwater is routinely used for crop irrigation in watershed, which can undergo subsequent Si uptake in the shallow soil depending on crop type. Additionally, for both watersheds we assume that the $\delta^{30}Si$ values of primary silicate minerals is similar to the bedrock value, which is not always the case. Recent mineral-specific isotopic analyses suggest that biotite exhibits a more negative $\delta^{30}Si$ values among the primary silicate minerals (ranging from −0.3 to −1.0 ‰, Frings et al., 2021), which makes biotite contribution to weathering flux an overestimate. Overall, the consistently low $\delta^{30}Si$ values in groundwater compared to soil porewaters in both the Berambadi and Mule Hole watersheds reflects that the signatures of weathering, biotic uptake and/or adsorption occurring at shallow soil horizons and are partly overwritten and homogenized by additional DSi fluxes (upto 50 % of groundwater DSi) from primary minerals weathering in the deep critical zone. The input of lighter Si from weathering in deeper layers of the regolith can also explain why groundwater systems are generally lower in $\delta^{30}Si$ compared to river water, the latter integrating signatures from shallow and deep-water solute fluxes.

## 5. Conclusion

We assessed the impact of land use changes on the silicon isotopic composition of groundwater by comparing two contrasting watersheds, the forested Mule Hole watershed and the cultivated Berambadi watershed. Contrary to dissolved silicon concentration, the $\delta^{30}Si$ signatures of groundwater indicates no significant impact of landuse, despite continuous crop cultivation for more than 30 years in Berambadi. Moreover, groundwater exhibits no seasonal differences in terms of $\delta^{30}Si$ composition, indicating that immediate monsoonal precipitation imparts little influence on the groundwater composition. The primary silicate weathering and formation of secondary minerals exert dominant control over the silicon isotopic composition of groundwater, following a steady-state open flow through model. Apart from weathering controls, shallow aquifers can be impacted by plant uptake, adsorption/desorption of oxyhydroxides and dissolution of secondary phases and exhibits variable $\delta^{30}Si$. The $\delta^{30}Si$ values of groundwater from both watersheds (1.1 ± 0.5 ‰, $n = 51$) were significantly lower than the soil pore water composition (1.6 ± 0.2 ‰, $n = 17$), reflecting contribution from deep weathering Si fluxes controlling the Si isotopic composition. Overall, weathering of dominant primary silicate minerals (Na-Plagioclase, biotite and chlorite) and formation of kaolinite and smectite type clay minerals in deeper layers of regolith contributes to 46 to 51 % of total Si flux in the forested Mule Hole and 34 to 38 % in the intensely cultivated Berambadi watershed. Groundwater supports the baseflow of rivers, especially during the dry season, with a chemical composition and isotopic signature very different from shallow surface and subsurface runoff. Our results highlight the importance of deep regolith weathering in determining groundwater silicon isotopic composition, overwriting the signatures of aboveground land use, human alterations, and shallow regolith processes.

## CRediT authorship contribution statement

**Sarath Pullyottum Kavil:** Writing – review & editing, Writing – original draft, Visualization, Investigation, Formal analysis,

Conceptualization. **Jean Riotte:** Writing – review & editing, Supervision, Methodology, Conceptualization. **Ramananda Chakrabarti:** Writing – review & editing, Supervision, Resources, Conceptualization. **Arnaud Dapoigny:** Resources, Methodology, Investigation, Formal analysis. **Véronique Vaury:** Resources, Methodology, Formal analysis. **Laurent Ruiz:** Writing – review & editing, Resources, Project administration. **Damien Cardinal:** Writing – review & editing, Supervision, Resources, Project administration, Methodology, Funding acquisition, Conceptualization.

## Declaration of competing interest

Damien Cardinal reports financial support was provided by CEFIPRA-IFCPAR. Sarath Pullyottum Kavil reports financial support was provided by IRD-Campus France. If there are other authors, they declare that they have no known competing financial interests or personal relationships that could have appeared to influence the work reported in this paper.

## Data availability

Data will be made available on request.

## Acknowledgments

The work is funded by CEFIPRA-IFCPAR support (NUNDERGROUND, project #5907). We acknowledge SNO M-TROPICS environmental observatory (https://mtropics.obs-mip.fr/) for providing necessary support for field campaign and sampling. Analysis of the isotopic composition of rainwater from Mule Hole were supported by the French programe INSU EC2CO. The authors thank Benjamin Baud for the water sampling during field work, Pierre Burckel and Irina Djouraev for the help with ICPMS analysis to check for validity of Si separation protocol and the ALYSES facility (IRD-SU). We thank Julien Amelin for providing the sampling map for Berambadi. SPK thank IRD-Campus France for providing Ph.D. scholarship and constant support to carry out the work. SPK also thanks Sourav Ganguly for his inputs and discussion. The authors would like to thanks M. Benrahmoune (LOCEAN-IPSL) for help in sample processing and clean lab management.

## Appendix A. Supplementary data

Supplementary data to this article can be found online at https://doi.org/10.1016/j.chemgeo.2024.122370.

## References

Abraham, K., Opfergelt, S., Fripiat, F., Cavagna, A.J., de Jong, J.T.M., Foley, S.F., André, L., Cardinal, D., 2008. $\delta^{30}$Si and $\delta^{29}$Si determinations on USGS BHVO-1 and BHVO-2 reference materials with a new configuration on a Nu plasma multi-collector ICP-MS. Geostand. Geoanal. Res. 32, 193–202.

Alexandre, A., Meunier, J.D., Colin, F., Koud, J.M., 1997. Plant impact on the biogeochemical cycle of silicon and related weathering processes. Geochim. Cosmochim. Acta 61, 677–682.

Barbiéro, L., Parate, H.R., Descloitres, M., Bost, A., Furian, S., Mohan Kumar, M.S., Kumar, C., Braun, J.J., 2007. Using a structural approach to identify relationships between soil and erosion in a semi-humid forested area, South India. Catena (Amst) 70, 313–329.

Bhaduri, A., Amarasinghe, U., Shah, T., 2012. An analysis of groundwater irrigation expansion in India. Int. J. Environ. Waste Manag. 9, 372–387.

Bouchez, J., Von Blanckenburg, F., Schuessler, J.A., 2013. Modeling novel stable isotope ratios in the weathering zone. Am. J. Sci. 313, 267–308.

Braun, J.J., Descloitres, M., Riotte, J., Fleury, S., Barbiéro, L., Boeglin, J.L., Violette, A., Lacarce, E., Ruiz, L., Sekhar, M., Mohan, Kumar M., S., Subramanian S. and Dupré B., 2009. Regolith mass balance inferred from combined mineralogical, geochemical and geophysical studies: Mule Hole gneissic watershed, South India. Geochim. Cosmochim. Acta 73, 935–961.

Buvaneshwari, S., Sekhar, M., Mohan Kumar, M.S., Giriraja, P.R., Buvaneshwari, S., Riotte, J., Sekhar, M., Mohan Kumar, M.S., Sharma, A.K., Duprey, J.L., Praveenkumarreddy, Y., Moger, H., Braun, J.J., Ruiz, L., Riotte, J., Audry, S., Braun, J.J., Durand, P., Ruiz, L., Sharma, A.K., 2017. Groundwater resource vulnerability and spatial variability of nitrate contamination: Insights from high density tubewell monitoring in a hard rock aquifer. Sci. Total Environ. 579, 838–847.

Buvaneshwari, S., Riotte, J., Sekhar, M., Sharma, A.K., Helliwell, R., Kumar, M.S.M., Braun, J.J., Ruiz, L., 2020. (2020) Potash fertilizer promotes incipient salinization in groundwater irrigated semi-arid agriculture. Sci. Report. 101 (10), 1–14.

Carey, J.C., Fulweiler, R.W., 2016. Human appropriation of biogenic silicon – the increasing role of agriculture. Funct. Ecol. 30, 1331–1339.

Chitra-Tarak, R., Ruiz, L., Dattaraja, H.S., Mohan Kumar, M.S., Riotte, J., Suresh, H.S., McMahon, S.M., Sukumar, R., 2018. The roots of the drought: Hydrology and water uptake strategies mediate forest-wide demographic response to precipitation. J. Ecol. 106, 1495–1507.

Clark, Ian, 2015. Groundwater Geochemistry and Isotopes. CRC press.

Closset, I., Cardinal, D., Rembauville, M., Thil, F., Blain, S., 2016. Unveiling the Si cycle using isotopes in an iron-fertilized zone of the Southern Ocean: from mixed-layer supply to export. Biogeosciences 13, 6049–6066.

Conley, D.J., Humborg, C., Smedberg, E., Rahm, L., Papush, L., Danielsson, Å., Clarke, A., Pastuszak, M., Aigars, J., Ciuffa, D., Mörth, C.M., 2008. Past, present and future state of the biogeochemical Si cycle in the Baltic Sea. J. Mar. Syst. 73, 338–346.

Cornelis, J.T., Delvaux, B., Georg, R.B., Lucas, Y., Ranger, J., Opfergelt, S., 2011. Tracing the origin of dissolved silicon transferred from various soil-plant systems towards rivers: A review. Biogeosciences 8, 89–112.

Craig, H., 1961. Isotopic variations in meteoric waters. Science (1979) 133, 1702–1703.

Delstanche, S., Opfergelt, S., Cardinal, D., Elsass, F., André, L., Delvaux, B., 2009. Silicon isotopic fractionation during adsorption of aqueous monosilicic acid onto iron oxide. Geochim. Cosmochim. Acta 73, 923–934.

Delvaux, C., Cardinal, D., Carbonnel, V., Chou, L., Hughes, H.J., André, L., 2013. Controls on riverine $\delta^{30}$Si signatures in a temperate watershed under high anthropogenic pressure (Scheldt — Belgium). J. Mar. Syst. 128, 40–51.

Dewandel, B., Lachassagne, P., Wyns, R., Maréchal, J.C., Krishnamurthy, N.S., 2006. A generalized 3-D geological and hydrogeological conceptual model of granite aquifers controlled by single or multiphase weathering. J. Hydrol. 330, 260–284.

Ding, T.P., Zhou, J.X., Wan, D.F., Chen, Z.Y., Wang, C.Y., Zhang, F., 2008. Silicon isotope fractionation in bamboo and its significance to the biogeochemical cycle of silicon. Geochim. Cosmochim. Acta 72, 1381–1395.

Druhan, J.L., Maher, K., 2017. The influence of mixing on stable isotope ratios in porous media: A revised Rayleigh model. Water Resourc. Res. 53 (2), 1101–1124. https://doi.org/10.1002/2016WR019666.

Dupuis, R., Benoit, M., Nardin, E., Méheut, M., 2015. Fractionation of silicon isotopes in liquids: the importance of configurational disorder. Chem. Geol. 396, 239–254.

Ehlert, C., Reckhardt, A., Greskowiak, J., Liguori, B.T.P., Böning, P., Paffrath, R., Brumsack, H.J., Pahnke, K., 2016. Transformation of silicon in a sandy beach ecosystem: Insights from stable silicon isotopes from fresh and saline groundwaters. Chem. Geol. 440, 207–218.

Epstein, E., Epstein, C.E., 2009. Silicon: its manifold roles in plants. Ann. Appl. Biol. 155, 155–160.

Evaristo, J., Jasechko, S., McDonnell, J.J., 2015. Global separation of plant transpiration from groundwater and streamflow. Nature 525 (7567), 91–94.

FAO-ISRIC-ISSS, 1998. World reference base for soil resources. In: World Soil Resources Report, 84. FAO, Rome.

Fernandez, N.M., Zhang, X., Druhan, J.L., 2019. Silicon isotopic re-equilibration during amorphous silica precipitation and implications for isotopic signatures in geochemical proxies. Geochim. Cosmochim. Acta 262, 104–127.

Fernandez, N.M., Bouchez, J., Derry, L.A., Chorover, J., Gaillardet, J., Giesbrecht, I., Fries, D., Druhan, J.L., 2022. Resiliency of silica export signatures when low order streams are subject to storm events. J. Geophys. Res. Biogeosci. 127 e2021JG006660.

Fischer, C., Aubron, C., Trouvé, A., Sekhar, M., Ruiz, L., 2022. Groundwater irrigation reduces overall poverty but increases socioeconomic vulnerability in a semiarid region of southern India. Sci. Report. 121 (12), 1–16.

Fishman, R.M., Siegfried, T., Raj, P., Modi, V., Lall, U., 2011. Over-extraction from shallow bedrock versus deep alluvial aquifers: Reliability versus sustainability considerations for India's groundwater irrigation. Water Resour. Res. 47.

Frick, D.A., Remus, R., Sommer, M., Augustin, J., Kaczorek, D., Von Blanckenburg, F., 2020. Silicon uptake and isotope fractionation dynamics by crop species. Biogeosciences 17, 6475–6490.

Frings, P.J., Clymans, W., Fontorbe, G., Gray, W., Chakrapani, G., Conley, D.J., De La Rocha, C., 2015. Silicate weathering in the Ganges alluvial plain. Earth Planet. Sci. Lett. 427, 136–148.

Frings, P.J., Clymans, W., Fontorbe, G., De La Rocha, C.L., Conley, D.J., 2016. The continental Si cycle and its impact on the ocean Si isotope budget. Chem. Geol. 425, 12–36.

Frings, P.J., Oelze, M., Schubring, F., Frick, D.A., von Blanckenburg, F., 2021. Interpreting silicon isotopes in the critical zone. Am. J. Sci. 321, 1164–1203.

Gaillardet, J., Dupré, B., Louvat, P., Allègre, C.J., 1999. Global silicate weathering and CO2 consumption rates deduced from the chemistry of large rivers. Chem. Geol. 159, 3–30.

Gaillardet, J., Braud, I., Hankard, F., Anquetin, S., Bour, O., Dorfliger, N., Dreuzy, J.R., Galle, S., Galy, C., Gogo, S., Gourcy, L., Habets, F., Laggoun, F., Longuevergne, L., Le, Borgne T., Naaim-Bouvet, F., Nord, G., Simonneaux, V., Six, D., Tallec, T., Valentin, C., Abril, G., Allemand, P., Arènes, A., Arfib, B., Arnaud, L., Arnaud, N., Arnaud, P., Audry, S., Comte, V.B., Batiot, C., Battais, A., Bellot, H., Bernard, E., Bertrand, C., Bessière, H., Binet, S., Bodin, J., Bodin, X., Boithias, L., Bouchez, J., Boudevillain, B., Moussa, I.B., Branger, F., Braun, J.J., Brunet, P., Caceres, B., Calmels, D., Cappelaere, B., Celle-Jeanton, H., Chabaux, F., Chalikakis, K.,

Champollion, C., Copard, Y., Cotel, C., Davy, P., Deline, P., Delrieu, G., Demarty, J., Dessert, C., Dumont, M., Emblanch, C., Ezzahar, J., Estèves, M., Favier, V., Faucheux, M., Filizola, N., Flammarion, P., Floury, P., Fovet, O., Fournier, M., Francez, A.J., Gandois, L., Gascuel, C., Gayer, E., Genthon, C., Gérard, M.F., Gilbert, D., Gouttevin, I., Grippa, M., Gruau, G., Jardani, A., Jeanneau, L., Join, J.L., Jourde, H., Karbou, F., Labat, D., Lagadeuc, Y., Lajeunesse, E., Lastennet, R., Lavado, W., Lawin, E., Lebel, T., Le, Bouteiller C., Legout, C., Lejeune, Y., Le, Meur E., Le, Moigne N., Lions, J., Lucas, A., Malet, J.P., Marais-Sicre, C., Maréchal, J.C., Marlin, C., Martin, P., Martins, J., Martinez, J.M., Massei, N., Mauclerc, A., Mazzilli, N., Molénat, J., Moreira-Turcq, P., Mougin, E., Morin, S., Ngoupayou, J.N., Panthou, G., Peugeot, C., Picard, G., Pierret, M.C., Porel, G., Probst, A., Probst, J.L., Rabatel, A., Raclot, D., Ravanel, L., Rejiba, F., René, P., Ribolzi, O., Riotte, J., Rivière, A., Robain, H., Ruiz, L., Sanchez-Perez, J.M., Santini, W., Sauvage, S., Schoeneich, P., Seidel, J.L., Sekhar, M., Sengtaheuanghoung, O., Silvera, N., Steinmann, M., Soruco, A., Tallec, G., Thibert, E., Lao, D.V., Vincent, C., Viville, D., Wagnon, P., Zitouna, R., 2018. OZCAR: the French network of critical zone observatories. Vadose Zo. J. 17, 1–24.

Geilert, S., Vroon, P.Z., Roerdink, D.L., Van Cappellen, P., van Bergen, M.J., 2014. Silicon isotope fractionation during abiotic silica precipitation at low temperatures: Inferences from flow-through experiments. Geochim. Cosmochim. Acta 142, 95–114.

Georg, R.B., Reynolds, B.C., Frank, M., Halliday, A.N., 2006a. New sample preparation techniques for the determination of Si isotopic compositions using MC-ICPMS. Chem. Geol. 235, 95–104.

Georg, R.B., Reynolds, B.C., Frank, M., Halliday, A.N., 2006b. Mechanisms controlling the silicon isotopic compositions of river waters. Earth Planet. Sci. Lett. 249, 290–306.

Georg, R.B., Reynolds, B.C., West, A.J., Burton, K.W., Halliday, A.N., 2007. Silicon isotope variations accompanying basalt weathering in Iceland. Earth and Planet. Sci. Lett. 261 (3–4), 476–490. https://doi.org/10.1016/J.EPSL.2007.07.004.

Georg, R.B., West, A.J., Basu, A.R., Halliday, A.N., 2009a. Silicon fluxes and isotope composition of direct groundwater discharge into the Bay of Bengal and the effect on the global ocean silicon isotope budget. Earth Planet. Sci. Lett. 283, 67–74.

Georg, R.B., Zhu, C., Reynolds, B.C., Halliday, A.N., 2009b. Stable silicon isotopes of groundwater, feldspars, and clay coatings in the Navajo Sandstone aquifer, Black Mesa, Arizona, USA. Geochim. Cosmochim. Acta 73, 2229–2241.

Gonfiantini, R., 1986. Environmental isotopes in lake studies. In: Fritz, P., Fontes, J.Ch. (Eds.), Handbook of Environmental Isotope Geochemistry. Elsevier, New York, pp. 113–168.

Good, S.P., Noone, D., Bowen, G., 2015. Hydrologic connectivity constrains partitioning of global terrestrial water fluxes. Science (1979) 349, 175–177.

Grasshoff, K., Kremling, K., Ehrhardt, M., 1999. Methods of Seawater Analysis, 3rd ed. Wiley-VCH, Weinheim, Germany.

Gunnell, Y., Bourgeon, G., 1997. Soils and climatic geomorphology on the Karnataka plateau, peninsular India. CATENA 29, 239–262.

Hughes, H.J., Delvigne, C., Korntheuer, M., De Jong, J., André, L., Cardinal, D., 2011. Controlling the mass bias introduced by anionic and organic matrices in silicon isotopic measurements by MC-ICP-MS. J. Anal. At. Spectrom. 26, 1892–1896.

Karl, D.M., Tien, G., 1992. MAGIC: A sensitive and precise method for measuring dissolved phosphorus in aquatic environments. Limnol. Oceanogr. 37, 105–116.

Maréchal, J.C., Varma, M.R.R., Riotte, J., Vouillamoz, J.M., Kumar, M.S.M., Ruiz, L., Sekhar, M., Braun, J.J., 2009. Indirect and direct recharges in a tropical forested watershed: Mule Hole, India. J. Hydrol. 364, 272–284.

Martin, A.N., Meredith, K., Baker, A., Norman, M.D., Bryan, E., 2021. The evolution of stable silicon isotopes in a coastal carbonate aquifer on Rottnest Island, Western Australia. Hydrol. Earth Syst. Sci. 25, 3837–3853. https://doi.org/10.5194/HESS-25-3837-2021.

Naqvi, S.M., Rogers, J.J.W., 1987. Precambrian Geology of India. Oxford University Press; Clarendon Press, Oxford, 223pp.

Oelze, M., von Blanckenburg, F., Bouchez, J., Hoellen, D., Dietzel, M., 2015. The effect of Al on Si isotope fractionation investigated by silica precipitation experiments. Chem. Geol. 397, 94–105.

Opfergelt, S., Delmelle, P., 2012. Silicon isotopes and continental weathering processes: Assessing controls on Si transfer to the ocean. Compt. Rendus Geosci. 344, 723–738.

Opfergelt, S., Cardinal, D., Henriet, C., Draye, X., André, L., Delvaux, B., 2006. Silicon isotopic fractionation by banana (Musa spp.) grown in a continuous nutrient flow device. Plant Soil 2851 (285), 333–345.

Opfergelt, S., Georg, R.B., Delvaux, B., Cabidoche, Y.M., Burton, K.W., Halliday, A.N., 2012. Silicon isotopes and the tracing of desilication in volcanic soil weathering sequences, Guadeloupe. Chem. Geol. 326–327, 113–122.

Opfergelt, S., Burton, K.W., Pogge von Strandmann, P.A.E., Gislason, S.R., Halliday, A.N., 2013. Riverine silicon isotope variations in glaciated basaltic terrains: Implications for the Si delivery to the ocean over glacial–interglacial intervals. Earth Planet. Sci. Lett. 369–370, 211–219.

Pogge von Strandmann, P.A.E., Porcelli, D., James, R.H., van Calsteren, P., Schaefer, B., Cartwright, I., Reynolds, B.C., Burton, K.W., 2014. Chemical weathering processes in the Great Artesian Basin: evidence from lithium and silicon isotopes. Earth Planet. Sci. Lett. 406, 24–36.

Pokrovsky, O.S., Reynolds, B.C., Prokushkin, A.S., Schott, J., Viers, J., 2013. Silicon isotope variations in Central Siberian rivers during basalt weathering in permafrost-dominated larch forests. Chem. Geol. 355, 103–116.

Rahman, S., Tamborski, J.J., Charette, M.A., Cochran, J.K., 2019. Dissolved silica in the subterranean estuary and the impact of submarine groundwater discharge on the global marine silica budget. Mar. Chem. 208, 29–42.

Reynolds, B.C., Aggarwal, J., André, L., Baxter, D., Beucher, C., Brzezinski, M.A., Engström, E., Georg, R.B., Land, M., Leng, M.J., Opfergelt, S., Rodushkin, I., Sloane, H.J., Boorn, S.H.J.M., van den, Vroon P. Z. and Cardinal D., 2007. An inter-laboratory comparison of Si isotope reference materials. J. Anal. At. Spectrom. 22, 561–568.

Riotte, J., Ruiz, L., Audry, S., Sekhar, M., Mohan Kumar, M.S., Siva Soumya, B., Braun, J. J., 2014. Impact of Vegetation and Decennial Rainfall Fluctuations on the Weathering Fluxes Exported from a Dry Tropical Forest (Mule Hole). Procedia Earth Planet. Sci. 10, 34–37.

Riotte, J., Meunier, J.D., Zambardi, T., Audry, S., Barboni, D., Anupama, K., Prasad, S., Chmeleff, J., Poitrasson, F., Sekhar, M., Braun, J.J., 2018a. Processes controlling silicon isotopic fractionation in a forested tropical watershed: Mule Hole critical Zone Observatory (Southern India). Geochim. Cosmochim. Acta 228, 301–319.

Riotte, J., Sandhya, K., Prakash, N.B., Audry, S., Zambardi, T., Chmeleff, J., Buvaneshwari, S., Meunier, J.D., 2018b. Origin of silica in rice plants and contribution of diatom Earth fertilization: insights from isotopic Si mass balance in a paddy field. Plant Soil 423, 481–501.

Riotte, J., Ruiz, L., Audry, S., Baud, B., Bedimo Bedimo, J.P., Boithias, L., Braun, J.J., Dupré, B., Duprey, J.L., Faucheux, M., Lagane, C., Marechal, J.C., Moger, H., Mohan Kumar, M.S., Parate, H., Ribolzi, O., Rochelle-Newall, E., Sriramulu, B., Varma, M., Sekhar, M., 2021a. The Multiscale TROPIcal CatchmentS critical zone observatory M-TROPICS dataset III: Hydro-geochemical monitoring of the Mule Hole catchment, South India. Hydrol. Process. 35, e14196.

Riotte, J., Ruiz, L., Audry, S., Baud, B., Bedimo Bedimo, J.P., Boithias, L., Braun, J.J., Dupré, B., Duprey, J.L., Faucheux, M., Lagane, C., Marechal, J.C., Moger, H., Mohan Kumar, M.S., Parate, H., Ribolzi, O., Rochelle-Newall, E., Sriramulu, B., Varma, M., Sekhar, M., 2021b. The multiscale TROPIcal CatchmentS critical zone observatory M-TROPICS dataset III: Hydro-geochemical monitoring of the Mule Hole catchment, South India. Hydrol. Process. 35, e14196.

Robert, M., Thomas, A., Sekhar, M., Badiger, S., Ruiz, L., Willaume, M., Leenhardt, D., Bergez, J.E., 2017. Farm typology in the berambadi watershed (India): farming systems are determined by farm size and access to groundwater. Water 9, 51, 9, 51.

Rodell, M., Velicogna, I., Famiglietti, J.S., 2009. Satellite-based estimates of groundwater depletion in India. Nat 999–1002, 2009 4607258 460.

Ruiz, L., Varma, M.R.R., Kumar, M.S.M., Sekhar, M., Maréchal, J.C., Descloitres, M., Riotte, J., Kumar, S., Kumar, C., Braun, J.J., 2010. Water balance modelling in a tropical watershed under deciduous forest (Mule Hole, India): Regolith matric storage buffers the groundwater recharge process. J. Hydrol. 380, 460–472.

Santos, J.C.B., Le Pera, E., Souza Júnior, V.S., Oliveira, C.S., Juilleret, J., Corrêa, M.M., Azevedo, A.C., 2018. Porosity and genesis of clay in gneiss saprolites: the relevance of saprolithology to whole regolith pedology. Geoderma 319, 1–13. https://doi.org/10.1016/J.GEODERMA.2017.12.031.

Sarath, P.K., Mangalaa, K.R., Cardinal, D., Gurumurthy, G.P., Dapoigny, A., Sarma, V.V. S.S., Riotte, J., 2022. Seasonal, weathering and water use controls of silicon cycling along the river flow in two contrasting basins of South India. Chem. Geol. 604, 120883. https://doi.org/10.1016/J.CHEMGEO.2022.120883.

Savage, P.S., Armytage, R.M.G., Georg, R.B., Halliday, A.N., 2014. High temperature silicon isotope geochemistry. Lithos 190–191, 500–519.

Sekhar, M., Riotte, J., Ruiz, L., Jouquet, P., Braun, J.J., 2016. Influences of climate and agriculture on water and biogeochemical cycles: Kabini critical zone observatory. Proc. Indian Natl. Sci. Acad. 82, 833–846.

Soumya, B.S., Sekhar, M., Riotte, J., Audry, S., Lagane, C., Braun, J.J., 2011. Inverse models to analyze the spatiotemporal variations of chemical weathering fluxes in a granito-gneissic watershed: Mule Hole, South India. Geoderma 165, 12–24.

Sprenger, M., Llorens, P., Cayuela, C., Gallart, F., Latron, J., 2019. Mechanisms of consistently disjunct soil water pools over (pore) space and time. Hydrol. Earth Syst. Sci. 23, 2751–2762. https://doi.org/10.5194/HESS-23-2751-2019.

Steinhoefel, G., Breuer, J., von Blanckenburg, F., Horn, I., Sommer, M., 2017. The dynamics of Si cycling during weathering in two small catchments in the Black Forest (Germany) traced by Si isotopes. Chem. Geol. 466, 389–402.

Stewart, B., Shanley, J.B., Kirchner, J.W., Norris, D., Adler, T., Bristol, C., et al., 2022. Streams as Mirrors: Reading Subsurface Water Chemistry From Stream Chemistry. Water Resourc. Res. 58 (1), e2021WR029931. https://doi.org/10.1029/2021WR029931.

Street-Perrott, F.A., Barker, P.A., 2008. Biogenic silica: a neglected component of the coupled global continental biogeochemical cycles of carbon and silicon. Earth Surf. Process. Landf. 33, 1436–1457.

Struyf, E., Smis, A., Van Damme, S., Garnier, J., Govers, G., Van Wesemael, B., Conley, D. J., Batelaan, O., Frot, E., Clymans, W., Vandevenne, F., Lancelot, C., Goos, P., Meire, P., 2010. Historical land use change has lowered terrestrial silica mobilization. Nat. Commun. 11 (1), 1–7.

Sun, Y., Wu, L., Li, X., Sun, L., Gao, J., Ding, T., Zhu, Y., 2017. Silicon Isotope Fractionation in Maize and its Biogeochemical significance. Anal. Lett. 50, 2475–2490.

Thenkabail, P.S., Biradar, C.M., Noojipady, P., Dheeravath, V., Li, Y., Velpuri, M., Gumma, M., Gangalakunta, O.R.P., Turral, H., Cai, X., Vithanage, J., Schull, M.A., Dutta, R., 2009. Global irrigated area map (GIAM), derived from remote sensing, for the end of the last millennium. Int. J. Remote Sens. 30, 3679–3733.

Tréguer, P.J., Sutton, J.N., Brzezinski, M., Charette, M.A., Devries, T., Dutkiewicz, S., Ehlert, C., Hawkings, J., Leynaert, A., Liu, S.M., Monferrer, N.L., López-Acosta, M., Maldonado, M., Rahman, S., Ran, L., Rouxel, O., 2021. Reviews and syntheses: the biogeochemical cycle of silicon in the modern ocean. Biogeosciences 18, 1269–1289.

Vandevenne, F.I., Barão, L., Ronchi, B., Govers, G., Meire, P., Kelly, E.F., Struyf, E., 2015. Silicon pools in human impacted soils of temperate zones. Glob. Biogeochem. Cycles 29, 1439–1450.

Violette, A., Goddéris, Y., Maréchal, J.C., Riotte, J., Oliva, P., Kumar, M.S.M., Sekhar, M., Braun, J.J., 2010. Modelling the chemical weathering fluxes at the watershed scale in the Tropics (Mule Hole, South India): Relative contribution of the smectite/kaolinite assemblage versus primary minerals. Chem. Geol. 277, 42–60.

Warrier, C. Unnikrishnan, Praveen Babu, M., Manjula, P., Velayudhan, K.T., Shahul Hameed, A., 2010. Isotopic Characterization of Dual Monsoon Precipitation – Evidence from Kerala, India. Current Sci. 98 (11), 1487–1495.

Zheng, X.Y., Beard, B.L., Johnson, C.M., 2019. Constraining silicon isotope exchange kinetics and fractionation between aqueous and amorphous Si at room temperature. Geochim. Cosmochim. Acta 253, 267–289.

Ziegler, K., Chadwick, O.A., White, A.F., Brzezinski, M.A., 2005. δ30Si systematics in a granitic saprolite, Puerto Rico. Geology 33, 817–820.